Pergamon

Geochimica et Cosmochimica Acta, Vol. 62, No. 8, pp. 1419–1442, 1998

0016-7037/98 $19.00 + .00

PII S0016-7037(98)00029-5

Mega-chondrules and large, igneous-textured clasts in Julesberg (L3) and other ordinary chondrites: Vapor-fractionation, shock-melting, and chondrule formation

ALEX RUZICKA,* GREGORY A. SNYDER, and LAWRENCE A. TAYLOR

Planetary Geosciences Institute, Department of Geological Sciences, University of Tennessee, Knoxville, Tennessee 37996-1410, USA

(*Received June* 4, 1997; *accepted in revised form November* 19, 1997)

Abstract—A petrographic-microprobe study of large, metal-poor, igneous-textured objects in Julesberg (L3) and other ordinary chondrites suggests that they can be classified into two petrographic types: mega-chondrules and large lithic clasts; and into two chemical types: Na-poor and Na-rich.

Mega-chondrules show textural evidence of having solidified as freely-floating melt droplets, whereas lithic clasts formed by the fragmentation of larger objects, possibly still larger mega-chondrules. Barred-olivine or barred-olivine-pyroxene textures are most common for mega-chondrules, whereas a variety of textures occur in large lithic clasts. The two petrographic types cannot be distinguished on the basis of modal, bulk, or phase compositions.

Sodium-poor objects are characterized by (1) plagioclase or glass with mainly bytownite composition ($An_{70\text{-}90}$ typical), (2) subchondritic Na/Al ratios and typically subchondritic volatile-element (Na, K, and Mn) abundances, and (3) bulk-chemical trends that resemble those expected for vapor-fractionation processes. Some Na-poor objects may have formed by the melting of precursors that formed as condensates or vaporization residues; others may have formed by the melting of precursors that formed by fractional condensation or fractional vaporization. Following vapor-fractionation, Na-poor objects or their precursors appear to have reequilibrated at lower temperatures, which raised the bulk Na content of the objects, but not to the levels seen in Na-rich objects. Enrichments of Fe^{2+}, Na, K, and P on the margins of some Na-poor objects suggest that they partly reacted with volatile-rich surroundings, both before and after brecciation. Sodium-rich objects are characterized by (1) plagioclase or glass with oligoclase or albite composition ($An_{2\text{-}25}$), (2) roughly chondritic Na/Al ratios and volatile-element (Na, K, Mn) abundances, and (3) bulk-chemical trends similar to those shown by melt-pocket glasses in ordinary chondrites. Sodium-rich melt objects could have formed by the shock-melting of chondritic precursors. Feldspathic compositions for some Na-rich melt objects can be explained by preferential shock-melting of feldspar or feldspathic glass in chondritic target materials.

Literature data imply that the same two chemical populations of objects, Na-poor and Na-rich, occur among smaller, normal-sized chondrules in Type 3 ordinary chondrites, suggesting that the same processes that affected large melt objects also affected chondrules.

1. INTRODUCTION

Many ordinary chondrites contain distinctively large, igneous-textured objects (large melt objects or inclusions) of obscure origin. These objects, which range up to a centimeter across or larger, are larger than normal-sized chondrules, which have typical diameters of ~0.3–0.9 mm in H-, L- and LL-group chondrites (Grossman et al, 1988). Besides their large sizes, many of the inclusions are also distinctive in having unusually low abundances of FeNi-metal and sulfide, often lower than in chondrules in the same meteorites.

Various models have been proposed for the formation of large melt objects. They could have formed by essentially whole-rock impact-melting of ordinary chondrite material, with subsequent loss of metal and sulfide (Fodor and Keil, 1976a,b; Dodd and Jarosewich, 1976; Keil et al., 1980), or by impact-melting of an already metal- and sulfide-depleted, chondrule-rich source (Rubin et al., 1981). An impact-melt origin for the inclusions would signify the importance of hypervelocity impacts in chondrite source regions. Another possibility is that the large melt objects are simply unusually large variants of normal-sized chondrules (Binns, 1967; Weisberg et al., 1988; Prinz et al., 1988), dubbed macrochondrules by some researchers (Weisberg et al., 1988; Prinz et al., 1988; Bridges and Hutchison, 1997). This would indicate that the chondrule-forming process was occasionally capable of producing melt volumes that are a factor of $\sim 10^2$–10^5 greater than those of typical chondrule melts. Finally, some of the inclusions may be fragments of igneous differentiates that formed through extensive melting of chondrite parent bodies (Hutchison et al., 1988, Kennedy et al., 1992; Ruzicka et al., 1995; Bridges et al., 1995) or by the remelting of igneous differentiates (Graham et al., 1976). If the inclusions are igneous differentiates, it would be evidence that chondrites, which most researchers consider to have formed exclusively from primitive nebular materials, also contain relatively evolved magmatic rocks.

The goals of this study were to (1) determine which processes were important in the formation of large melt inclusions and (2) determine whether the large melt objects are related to normal-sized chondrules. We surveyed large melt objects in polished thin sections and in handspecimens and performed detailed petrographic and electron microprobe studies of selected inclusions from various ordinary chondrites. For the purposes of this study, we considered any igneous-textured,

* Author to whom correspondence should be addressed (aruzicka@utk.edu).

Table 1. Large melt objects in ordinary chondrites.

object §	host	section
Jl-1	Julesberg (L3.6)	AMNH 4599-3
Jl-2	Julesberg (L3.6)	AMNH 4599-3
Jl-3 [1]	Julesberg (L3.6)	AMNH 4599-2
Jl-4	Julesberg (L3.6)	AMNH 4599 (slab C)
Jl-5	Julesberg (L3.6)	AMNH 4599 (slab C)
Jl-6	Julesberg (L3.6)	AMNH 4599 (slab B)
Jl-7	Julesberg (L3.6)	AMNH 4599 (slab B)
Jl-9	Julesberg (L3.6)	AMNH 4599 (slab B)
Jl-10	Julesberg (L3.6)	AMNH 4599 (slab B)
Jl-11	Julesberg (L3.6)	AMNH 4599 (slab B)
Jl-12	Julesberg (L3.6)	AMNH 4599 (slab B)
Jl-13	Julesberg (L3.6)	AMNH 4599 (slab B)
Jl-14	Julesberg (L3.6)	AMNH 4599 (slab B)
Jl-15	Julesberg (L3.6)	AMNH 4599 (slab B)
Jl-16	Julesberg (L3.6)	AMNH 4599 (slab A)
Jl-17	Julesberg (L3.6)	AMNH 4599 (slab A)
Jl-18	Julesberg (L3.6)	AMNH 4599 (slab A)
Jl-19	Julesberg (L3.6)	AMNH 4599 (slab A)
Jl-20	Julesberg (L3.6)	AMNH 4599 (slab A)
Bo-1 [2]	Bovedy (L3-4)	UA 144-1
Ca-1 [3]	Carraweena (L3)	AMNH 3902-1
Co-1	Cook (H5)	AMNH 4730-1
Et-1 [4]	Etter (L5)	AMNH 4462-1
Ev-1 [5]	Eva (H4)	AMNH 4368-1
Gu-1 [6]	Gunlock (L3.4)	AMNH 4620-3
Ho-1	Homestead (L5)	AMNH 3853-1
Vi-1	Vishnupur (LL4-6)	AMNH 4247-3
Vi-2 [7]	Vishnupur (LL4-6)	USNM 6007-1

§ In handspecimen, Jl-5, Jl-7, Jl-16, Jl-17, Ev-1, and Gu-1 appear dark-colored, and other objects appear light-colored. Dominantly light-colored Co-1 contains dark patches that correspond to melt pockets. [1] Object "Ju-1" of Weisberg et al. (1988). [2] Object "Bo-1" of Ruzicka et al. (1995). [3] Object "Ca-1" of Weisberg et al. (1988). [4] Object "Et-1" of Weisberg et al. (1988). [5] "Spinifex-textured clast" of Fodor and Keil (1976). [6] "Golfball-sized chondrule" of Prinz et al. (1988). [7] "Orthoclase-pyroxene fragment" of Wloztka et al. (1983).

metal- and sulfide-poor object that is >2 mm across and atypically large for the host meteorite to be a large melt object or inclusion. This specifically excludes large clasts with chondritic textures. A list of some of the inclusions we studied is given in Table 1.

We began this study with the belief that at least some large melt inclusions in ordinary chondrites are igneous differentiates (Ruzicka et al., 1995). However, we now believe that the other two models, involving chondrule formation and impact melting, are more viable. Despite a possible connection to chondrule-forming processes, the large melt objects do not easily fit into chondrule classification schemes based on olivine and feldspathic glass compositions (DeHart et al., 1992) or textures, mineral compositions, and modal mineralogy (Scott and Taylor, 1983; Scott et al., 1994). Moreover, the large sizes of the melt inclusions make them relatively amenable to study, and possibly less susceptible than chondrules to chemical modification by diffusional exchange with external environments. For these reasons, if large melt objects formed by processes related to chondrule formation, they may provide important insights into chondrule-forming processes that are not otherwise apparent.

2. EXPERIMENTAL TECHNIQUES AND SAMPLES

2.1. Experimental Techniques

An electron microprobe (Cameca SX-50) in the Department of Geological Sciences was used for quantitative phase analyses, x-ray mapping, and for backscattered-electron (BSE) studies. A scanning-electron-microscope (Hitachi S-3200N) in the Department of Biochemistry and Cellular and Molecular Biology was used for additional BSE studies.

Quantitative phase analyses were obtained with the microprobe by using wavelength-dispersive techniques, an accelerating voltage of 15 keV, and calibrations based on natural and synthetic mineral standards. The beam size and sample current was varied according to the phase being analyzed, to optimize counting statistics and minimize beam-induced element mobilization. For most phases, a focussed (~1 μm diameter) beam and a 30 na sample current gave good results. For analyses of feldspar and calcic glasses, the beam was expanded somewhat (~10 μm diameter), and the sample current was lowered to 10 na. For analyses of sodic glasses and nephelinitic material, the beam was enlarged still further (~15 μm diameter) and the sample current was reduced to 5 na. Analyses were deemed acceptable if the analysis total ranged between 98 and 101 wt% and the analysis stoichiometry was reasonable (3.00 $\pm$ 0.01 cations/4 oxygen for olivine, 4.00 $\pm$ 0.01 cations/6 oxygen for pyroxene, and 5.00 $\pm$ 0.025 cations/8 oxygen for feldspar). Between 5 and 50 acceptable analyses were obtained for each of the major phases (olivine, low-Ca-pyroxene, high-Ca pyroxene, feldspar, feldspathic glass) in each large melt object, with the number depending on phase heterogeneity. Selected analyses were also obtained for Cr-spinel, ilmenite, tridymite, Si-rich glass, FeNi metal, and troilite.

Modal analyses of the objects were obtained with the microprobe using a digital x-ray mapping technique (Taylor et al., 1996). With this technique, a focussed electron beam (3 na beam current, 20 keV accelerating voltage) was rastered in a 128 x 128 point grid pattern over a specified area. Typically, the area covered was 0.94 x 0.94 mm square, and the analysis spacing was ~7 μm. X-ray counts were obtained with an Oxford (Link) Instruments Energy Dispersive Spectrometer (EDS) eXL II at each point (pixel) in the grid, at wavelengths corresponding to K_α peaks for Na, Mg, Al, Si, P, S, K, Ca, Ti, Cr, Fe, and Ni. Each point was analyzed for 100 ms (dwell time). Using the Multi-image Phase Analysis software supplied by Oxford Instruments, the x-ray intensities for various elements were used to classify each pixel as corresponding to one of several phases, including olivine, low-Ca pyroxene ($<Wo_{20}$), high-Ca pyroxene ($>Wo_{20}$), phosphate, Fe-Ni metal, troilite, Cr-spinel, ilmenite, plagioclase, K-feldspar, Si-polymorph, feldspathoid, and voids. Trial-and-error was used to devise the optimal criteria for classifying phases in each object (Taylor et al., 1996). Petrographic and quantitative microprobe data were used to distinguish between feldspar and feldspathic glass, and between Si-polymorph and Si-glass. The proportion of phases in each area was determined by summing all of the classified pixels for a particular phase and dividing by the total number of classified pixels. Data for different areas in the same object were then averaged to obtain the

Table 2. Assignment of large, igneous-textured and metal-poor objects in ordinary chondrites to chemical and textural/shape groups. †

	Na-poor	Na-rich
mega-chondrules	Jl-2, Jl-3, Jl-9 Jl-12, Jl-13, Jl-15 Jl-18, Ho-1	Jl-17, Ca-1
lithic clasts	Jl-1, Jl-4, Jl-6 Jl-10, Jl-11, Jl-14 Jl-16, Jl-19, Jl-20 Bo-1, Vi-2*	Jl-5, Jl-7, Et-1 Vi-1, Ev-1, Gu-1

† *Chemical groups*: Na-poor objects have bulk Na/Al < chondrites and contain plagioclase or glass with predominantly bytownitic composition; Na-rich objects have bulk Na/Al ~ chondrites and contain feldspar or glass with albite-oligoclase composition. *Textural/shape groups*: mega-chondrules are objects that show textural evidence of having crystallized as free-floating droplets; lithic clasts show no such evidence and appear to have formed by the fragmentation of larger objects.
* Atypical Na-poor object.

mode for the object. Roughly 20–60% of the exposed surfaces of the objects were included in the x-ray mapping areas, enough to ensure a representative sampling of the objects. Based on varying the criteria for phase selection, the relative precision of the modal data for most phases is ~2–5% of the amount present. For Jl-4 and Jl-5 only, modes were determined on the basis of different brightness levels in digital BSE images, using the image-processing software, NIH Image 1.54.

The major-element bulk compositions of the objects were calculated by combining modal data with phase compositional data. Often, minor phases such as chromite and ilmenite were not analyzed, and in these cases, the chromite composition appropriate to L3 chondrites (Bunch et al., 1967) was assumed for Cr-spinel, and the ilmenite composition appropriate to ordinary chondrites (Snetsinger and Keil, 1969) was assumed for ilmenite. For other minor phases such as troilite, phosphate, and metal, the following compositions were assumed: (1) stoichiometric FeS for troilite, (2) the average composition of merrillite in type 6 ordinary chondrites (Van Schmus and Ribbe, 1969) for phosphate, and (3) metal with a weight proportion Fe:Ni = 86:14, which corresponds to the average composition of metal in L chondrites (Jarosewich, 1990), for FeNi-metal. Metal compositions vary from grain to grain, but the assumption of a constant Fe/Ni ratio for metal does not significantly affect the calculated bulk composition of the objects, owing to the small amount of metal present.

Most previous studies of large melt objects have employed microprobe defocussed beam analysis (DBA) to estimate bulk compositions. The DBA technique, while relatively rapid, is subject to inaccuracies that arise by analyzing inhomogeneous targets (Albee et al., 1977; Warren, 1997). Besides these inaccuracies, which for each element may be on the order of a few percent (Albee et al., 1977) or even larger (Warren, 1997), many defocussed beam analyses of large melt objects reported in the literature appear to be additionally compromised. Literature data for the bulk compositions of large melt objects show that the principal chemical variation is in FeO. The variation in FeO is large (from ~0 to ~30 wt%), but it is not strongly correlated with variations in other elements. Most likely, the variation in FeO is an artifact, produced by including x-ray counts of Fe from metal and sulfide with those from silicates, as per the DBA technique. For large melt objects that contain virtually all of their Fe in the form of silicate, such an error would not arise. However, some of the objects studied in the literature evidently contain significant proportions of sulfide or FeNi-metal, and for these objects, proper assignment of Fe to the various phases is crucial.

2.2. Samples

Most of our detailed work focussed on large melt objects in a single meteorite, the Julesberg (L3.6) chondrite (Graham, 1993; Sears et al., 1991), for several reasons. First, our survey revealed that Julesberg contains an unusually high number of large melt objects, as previously noted by Graham (1993). Both light- and dark-colored objects are present (Graham, 1993; Table 1). Second, Julesberg belongs to petrographic type 3 and so is relatively unmetamorphosed, although it was shock-metamorphosed to a moderate extent, corresponding to shock stage S3 (Rubin, 1994). Finally, samples of Julesberg appropriate to a petrographic-microprobe study were available for analysis. These samples included three thin sections and three slabs that were kindly made available by Dr. Martin Prinz. For Julesberg, we obtained detailed data for the nineteen largest large melt objects (designated Jl-1 through Jl-20; study of Jl-8 was limited by sample plucking). Julesberg contains dark-colored, sharply-defined shock-melt veins and more diffuse, large (≤2.5 cm-diameter) shock-melted zones. One such melt zone (~1 × 2 cm-diameter) dominates thin-section AMNH 4599-1. The large melt objects of this study are not concentrated near the shock-veins or large shock-melt regions, although the dark-colored melt objects are similar to the large shock-melted regions in terms of overall color, and, in one case (Jl-7), texture and composition. The large shock-melt regions may correspond to the large (≤4.5 cm-diameter), dark-colored clasts in Julesberg noted by Graham (1993), and interpreted by him to be impact melts.

In addition, we report detailed data on three additional large melt objects from more heavily metamorphosed ordinary chondrites, including one object each from Etter (Et-1; host H5), Homestead (Ho-1; host L5), and Vishnupur (Vi-1; host nominally LL6, but considered here to be genomict and reclassified as LL4-6).

Table 3a. Petrographic and mineral-chemical data for Na-rich, large melt objects.

object	diameter † (mm)	texture & type §	phase composition § ¶ (mol%)
		Na-rich clasts and mega-chondrules	
Jl-5	5.5 x 4.8	ol vitrophyre lithic clast	*ol* **Fa 24.0** ± 0.7 *gl** **An 10-25 Or 2-4 Ab 73-86**
Jl-7	4.0 x 3.0	clast-laden lithic clast	*ol* **Fa 23.0** ± 0.6 *opx* **Wo 0.5** ± 0.2 **En 90.9** ± 2.1 **Fs 8.6** ± 2.0 *gl* **An 10.4** ± 5.0 **Or 3.4** ± 1.2 **Ab 86.2** ± 4.0
Jl-17	4.8 x 3.0	cryptocrystalline mega-chondrule	*ol* **Fa 23.4** ± 0.6 *pig* **Wo 6.3** ± 1.4 **En 72.7** ± 1.7 **Fs 21.1** ± 1.0 *gl** **An 2-8 Or 1-8 Ab 90-96**
Et-1	≥13 x 8	ol microporphyry lithic clast	*ol* **Fa 24.7** ± 0.5 *opx* **Wo 1.4** ± 0.7 **En 77.0** ± 1.6 **Fs 21.6** ± 1.8 *diop* **Wo 44.0** ± 0.9 **En 46.9** ± 0.5 **Fs 9.1** ± 1.3 *plag* **An 13.4** ± 1.7 **Or 1.5** ± 1.1 **Ab 85.1** ± 1.4 *kfeld* **An 1.4** ± 1.4 **Or 23.8** ± 5.3 **Ab 74.8** ± 4.9
Vi-1	4.0 x 2.0	poik. ol-diop-feld lithic clast	*ol* **Fa 30.9** ± 0.3 *opx* **Wo 2.7** ± 0.8 **En 70.7** ± 1.7 **Fs 26.5** ± 1.0 *diop* **Wo 41.4** ± 1.4 **En 46.8** ± 0.7 **Fs 11.8** ± 0.7 *plag* **An 10.0** ± 3.0 **Or 2.9** ± 0.6 **Ab 87.1** ± 2.5
Ev-1	≥ 5.0	ol vitrophyre lithic clast	*ol** **Fa 8-13** [1]
Gu-1	>20 x >13	ol microporphyry lithic clast	*ol** **Fa 18-25** [2]
Ca-1	10.0 x >6.5	barred ol mega-chondrule	*ol** **Fa 19** [3]

† Apparent diameter in thin-section or on slab surface. § ol = olivine; px = pyroxene; feld = feldspar; trid = tridymite; orth = orthoclase; opx = low-Ca pyroxene (Wo ≤ 5); pig = pigeonite; aug = augite; diop = diopside; plag = plagioclase; kfeld = potassic feldspar; gl = feldspathic glass. ¶ Average (mean) and standard deviation. Fa = 100 Fe/(Mg+Fe); Wo = 100 Ca/(Mg+Fe+Ca); En = 100 Mg/(Mg+Fe+Ca); Fs = 100 Fe/(Mg+Fe+Ca); An = 100 Ca/(Ca+Na+K); Or = 100 K/(Ca+Na+K); Ab = 100 Na/(Ca+Na+K). *Approximate composition. [1] Fodor and Keil (1976). [2] Prinz et al. (1988). [3] Weisberg et al. (1988).

Table 3b. Petrographic and mineral-chemical data for Na-poor, large melt objects.

object	diameter † (mm)	texture & type §	phase composition § ¶ (mol%)
		Na-poor clasts and mega-chondrules	
Jl-1	4.5 x 3.5	ol microporphyry lithic clast	*ol* **Fa 16.8** ± 4.7 *pig* **Wo 11.2** ± 4.0 **En 73.3** ± 5.7 **Fs 15.5** ± 2.5 *plag* **An 79.8** ± 2.0 **Or 0.3** ± 0.1 **Ab 19.9** ± 2.0
Jl-2	8.0 x 6.0	barred ol-px mega-chondrule	*ol* **Fa 21.0** ± 0.7 *opx* **Wo 2.3** ± 1.3 **En 83.5** ± 5.0 **Fs 14.2** ± 4.0 *pig* **Wo 14.1** ± 10.1 **En 68.6** ± 6.5 **Fs 17.3** ± 3.7 plag **An 85.2** ± 0.9 **Or 0.3** ± 0.1 **Ab 14.5** ± 2.7
Jl-3	8.2 x 6.5	barred ol-px mega-chondrule	*ol* **Fa 20.8** ± 2.0 *opx* **Wo 2.4** ± 0.5 **En 79.0** ± 1.2 **Fs 18.5** ± 0.8 *aug* **Wo 26.8** ± 7.8 **En 52.4** ± 6.2 **Fs 20.8** ± 3.5 *gl* **An 80.5** ± 14.5 **Or 0.7** ± 1.6 **Ab 18.8** ± 13.0
Jl-4	5.1 x 4.1	granular ol lithic clast	*ol* **Fa 21.2** ± 1.4 *opx* **Wo 3.8** ± 0.3 **En 81.4** ± 0.7 **Fs 14.8** ± 0.8 *pig* **Wo 16.1** ± 6.0 **En 70.3** ± 5.2 **Fs 13.6** ± 1.5 *plag* **An 83.9** ± 2.9 **Or 0.2** ± 0.1 **Ab 15.8** ± 2.8
Jl-6	8.0 x 5.0	barred ol-px lithic clast	*ol* **Fa 21.4** ± 1.0 *opx* **Wo 1.5** ± 0.9 **En 82.4** ± 2.2 **Fs 16.2** ± 1.7 *pig* **Wo 19.6** ± 9.9 **En 57.1** ± 9.6 **Fs 23.4** ± 5.7 *plag* **An 80.5** ± 6.5 **Or 0.4** ± 0.2 **Ab 19.2** ± 6.4 *gl* **An 85.1** ± 2.5 **Or 0.3** ± 0.1 **Ab 14.6** ± 2.5
Jl-9	4.5 x 2.0	barred ol mega-chondrule	*ol* **Fa 15.1** ± 3.6 *pig* **Wo 15.3** ± 11.7 **En 76.7** ± 10.8 **Fs 7.9** ± 1.6 *plag* **An 79.2** ± 3.9 **Or 0.7** ± 0.5 **Ab 20.1** ± 3.4
Jl-10	3.3 x 2.0	granular px lithic clast	*opx* **Wo 1.4** ± 0.5 **En 71.3** ± 5.9 **Fs 27.3** ± 5.5 *pig* **Wo 6.0** ± 2.5 **En 50.6** ± 6.7 **Fs 43.4** ± 4.3 *plag* **An 79.5** ± 5.6 **Or 0.4** ± 0.2 **Ab 20.1** ± 5.4
Jl-11	2.7 x 2.3	anhedral ol-px lithic clast	*ol* **Fa 20.8** ± 2.6 *opx* **Wo 3.6** ± 1.6 **En 72.7** ± 5.6 **Fs 23.7** ± 4.7 *pig* **Wo 7.9** ± 1.0 **En 63.7** ± 4.9 **Fs 28.4** ± 4.2 *gl* **An 86.7** ± 1.6 **Or 0.3** ± 0.1 **Ab 12.9** ± 1.6
Jl-12	2.5 x 1.4	radial px mega-chondrule	*opx* **Wo 3.7** ± 0.7 **En 68.0** ± 1.7 **Fs 28.3** ± 1.2 *pig* **Wo 8.0** ± 1.8 **En 60.5** ± 4.0 **Fs 27.9** ± 8.3 *gl* **An 73.6** ± 1.8 **Or 0.4** ± 0.1 **Ab 26.0** ± 1.7
Jl-13	2.4 x 1.8	barred ol-px mega-chondrule	*ol* **Fa 22.9** ± 0.4 *opx* **Wo 3.6** ± 1.2 **En 87.1** ± 3.2 **Fs 9.4** ± 2.7 *diop* **Wo 30.3** ± 9.6 **En 65.1** ± 8.3 **Fs 4.7** ± 1.4 *plag* **An 82.9** ± 2.0 **Or 0.3** ± 0.1 **Ab 16.7** ± 1.9 gl **An 74.9** ± 3.9 **Or 0.4** ± 0.1 **Ab 24.7** ± 3.9
Jl-14	2.1 x 1.2	granular ol lithic clast	*ol* **Fa 22.1** ± 1.2 *pig* **Wo 7.8** ± 2.1 **En 82.1** ± 2.5 **Fs 10.1** ± 0.8 *plag* **An 79.6** ± 6.4 **Or 0.5** ± 0.1 **Ab 20.0** ± 6.3 *gl* **An 74.8** ± 5.4 **Or 0.7** ± 0.2 **Ab 24.6** ± 5.2
Jl-15	2.7 x 2.7	barred ol mega-chondrule	*ol* **Fa 23.1** ± 1.1 *pig* **Wo 12.9** ± 4.5 **En 68.1** ± 4.3 **Fs 19.0** ± 1.0 *gl* **An 79.1** ± 2.8 **Or 0.2** ± 0.1 **Ab 20.7** ± 2.8

(Continued.)

3. RESULTS AND DISCUSSION

3.1. Classification

Large melt objects in ordinary chondrites can be classified using a two-fold scheme according to their textures, shapes, and chemical compositions (Table 2). Two textural/shape types, mega-chondrules and large lithic clasts, can be discriminated based on petrographic criteria. Microprobe or bulk-chemical data can, in turn, be used to assign objects into one of two chemical groups, Na-poor and Na-rich. Mega-chondrules and lithic clasts both contain representatives of Na-poor and Na-rich groups.

Inclusion Vi-2, the orthoclase-pyroxene fragment of Wloztka et al. (1983), is here classified as a Na-poor lithic clast (Table 2), but it may be an example of a large melt object more properly assigned to a third chemical group. The K-rich composition for this object is unlike that of other large melt objects we studied.

3.2. Petrography

Table 3 summarizes petrographic and mineral-chemical data for large melt objects, and Figs. 1–3 illustrate some of the textures of these objects.

3.2.1. Mega-chondrules

Mega-chondrules show mainly barred-olivine or barred-olivine-pyroxene textures. Except for their large sizes, barred mega-chondrules are texturally similar to normal-sized, barred-olivine chondrules (Weisberg, 1987; Weisberg et al., 1988). In barred objects, a shell of olivine forms part of the perimeter of the objects, and sometimes an olivine shell also occurs concentrically within the object (Fig. 1a). In barred-olivine mega-chondrules, parallel bars of olivine are separated by feldspathic glass, or by a pyroxene- and feldspar-bearing mesostasis (Fig. 1e). In barred-olivine-pyroxene mega-chondrules, olivine is overgrown by low-Ca pyroxene (orthopyroxene or pigeonite) which comprises a large portion of the object (Fig. 1a, 1c).

Other textures found for mega-chondrules include radial-pyroxene (Jl-12) and cryptocrystalline (Jl-17). Jl-12 consists largely of low-Ca pyroxene with interstitial silica and feldspathic glasses, and completely lacks olivine (Fig. 1d). In this object, elongate or tabular low-Ca pyroxene grains are arranged

Table 3b, continued.

object	diameter † (mm)	texture & type §	phase composition § ¶ (mol%)
		Na-poor clasts and mega-chondrules	
Jl-16	11.0 x 9.0	granular/poik. lithic clast	ol **Fa 23.7** ± 1.3 *pig* **Wo 12.3** ± 4.7 **En 67.0** ± 4.7 **Fs 20.8** ± 2.2 *aug* **Wo 32.7** ± 1.5 **En 52.2** ± 1.2 **Fs 15.1** ± 1.3 *plag* **An 82.7** ± 2.2 **Or 0.3** ± 0.2 **Ab 17.0** ± 2.1
Jl-18	4.2 x 2.5	barred ol mega-chondrule	*ol* **Fa 20.7** ± 2.9 *pig* **Wo 11.6** ± 3.6 **En 81.3** ± 4.3 **Fs 7.2** ± 1.9 *aug* **Wo 28.9** ± 4.4 **En 65.6** ± 3.9 **Fs 5.5** ± 1.5 *gl* **An 83.1** ± 2.0 **Or 0.4** ± 0.2 **Ab 16.5** ± 2.0
Jl-19	4.2 x 2.5	ol microporphyry lithic clast	*ol* **Fa 19.9** ± 2.2 *opx* **Wo 3.5** ± 0.3 **En 85.5** ± 0.9 **Fs 10.9** ± 1.0 *pig* **Wo 11.8** ± 4.4 **En 76.4** ± 4.5 **Fs 11.8** ± 1.2 *aug* **Wo 33.3** ± 4.2 **En 57.9** ± 4.3 **Fs 8.9** ± 0.2 *plag* **An 82.1** ± 1.1 **Or 0.3** ± 0.1 **Ab 17.6** ± 1.1
Jl-20	3.6 x 2.5	px-rich poik. lithic clast	*ol* **Fa 17.6** ± 4.3 *opx* **Wo 2.5** ± 0.9 **En 88.9** ± 1.2 **Fs 8.7** ± 1.7 *pig* **Wo 13.4** ± 1.3 **En 69.5** ± 1.3 **Fs 17.3** ± 0.1 *aug* **Wo 29.5** ± 1.9 **En 59.6** ± 1.9 **Fs 11.0** ± 0.1 *plag* **An 69.5** ± 3.8 **Or 0.5** ± 0.1 **Ab 30.0** ± 3.8
Ho-1	7.0 x 4.5	barred ol-px mega-chondrule	*ol* **Fa 23.2** ± 0.6 *opx* **Wo 3.1** ± 2.0 **En 78.3** ± 2.0 **Fs 18.6** ± 1.7 *diop* **Wo 46.7** ± 2.7 **En 46.3** ± 1.7 **Fs 7.0** ± 1.3 *plag* **An 55.0** ± *13.8* **Or 1.0** ± 0.6 **Ab 43.9** ± 13.2
Bo-1	7.0 x 4.5	granular px lithic clast	*opx** **Wo 0.2-3 En 92-74 Fs 8-23** [4] *plag** **An 77-66 Or 0.3-2.2 Ab 23-32** [4]
Vi-2	2.0 x 1.4	poik. opx-trid-orth lithic clast	*opx** **Wo 3 En 61 Fs 36** [5] *aug** **Wo 41 En 41 Fs 18** [5] *kfeld** **An 1 Or 96 Ab 3** [5]

†, §, ¶, * As for Table 3a. [4] Ruzicka et al. (1995). [5] Wlotzka et al. (1983).

in a radial or fan-shape pattern, radiating away from a single point near the margin of the object, suggesting initial nucleation at that point.

Some mega-chondrules show distinctive core-to-rim variations in textures, in which barred cores are surrounded by granular mantles (Fig. 1b). Typically, there is no change in mineralogy from core to mantle, although one object (Jl-2) contains a higher proportion of metal and troilite in the mantle, and another (Jl-17) contains a mantle with a lower proportion of low-Ca pyroxene, and a higher proportion of glass and olivine, than in the interior of the object.

The textures of mega-chondrules clearly indicate that they solidified as free-floating droplets. The thick, outermost olivine shells of barred mega-chondrules and the fan-shaped arrangement of pyroxene grains in Jl-12 both suggest crystal nucleation at pre-existing margins of these objects. The core-to-rim textural variations of mega-chondrules are suggestive either of successive growth stages of individual droplets, or of the influence of the external medium surrounding the objects. All mega-chondrules have partly preserved, smooth, curved margins that undoubtedly represent a droplet surface, but most mega-chondrules experienced one or more brecciation events that partly removed this surface.

3.2.2. Large lithic clasts

Large lithic clasts lack smooth, curving boundaries or any evidence of core-mantle structures. They have irregular margins (Fig. 2a), suggesting that they formed by the fragmentation of even larger precursors. The textures of large lithic clasts vary more widely than for mega-chondrules, and include olivine microporphyry (Fig. 2a-b, 3a-b), granular olivine, granular pyroxene (Fig. 2c), vitrophyric (Fig. 2d), clast-laden (Fig. 2e), poikilitic (Fig. 2f), barred-olivine-pyroxene, and an olivine-pyroxene object with anhedral texture (Jl-11). The large lithic clast with barred-olivine-pyroxene texture (Jl-6) is probably a mega-chondrule fragment. Some large lithic clasts display variations in internal textures that do not form a core-mantle structure. For example, Et-1 and Jl-16 locally contain barred regions (barred-olivine) in addition to regions of microporphyritic or granular texture, and Jl-16 locally exhibits a poikilitic texture.

The olivine microporphyry and granular olivine textures shown by some large lithic clasts resemble those observed in many chondrules, although the olivine microphenocrysts in Jl-1 are unusually coarse (up to ~800 μm across; Fig. 2b), and the olivine grains in microporphyry Gu-1 (Fig. 3b) are often attached in groups to form a glomerocrystic texture not usually observed in chondrules. Other large lithic clasts have textures generally unlike those seen in chondrules. These include the clast-laden texture of Jl-7 (Fig. 2e; see below), the olivine vitrophyric (komatiitic) texture of Ev-1 (Fodor and Keil, 1976b), and the unusually coarse, holocrystalline textures of Vi-1 (Fig. 2f) and Vi-2 (Wloztka et al., 1983). Clasts Jl-10 (Fig. 2c) and Bo-1 (Ruzicka et al., 1995) are distinctive in containing large expanses of granular low-Ca pyroxene grains separated by tridymite laths and interstitial feldspar, a texture and assemblage atypical of chondrules.

Although the margin of Gu-1 is generally curved and in this way resembles that of a chondrule (Prinz et al., 1988), it is not analogous to the curved surfaces of mega-chondrules. In the mega-chondrules of this study, the curved surfaces acted as nucleation sites for phases to grow into the objects, whereas in Gu-1, the curved surface is delineated by a shock-melt vein that truncates the object (Fig. 3b). For this reason, we classify Gu-1 as a lithic clast, despite its generally curved margin.

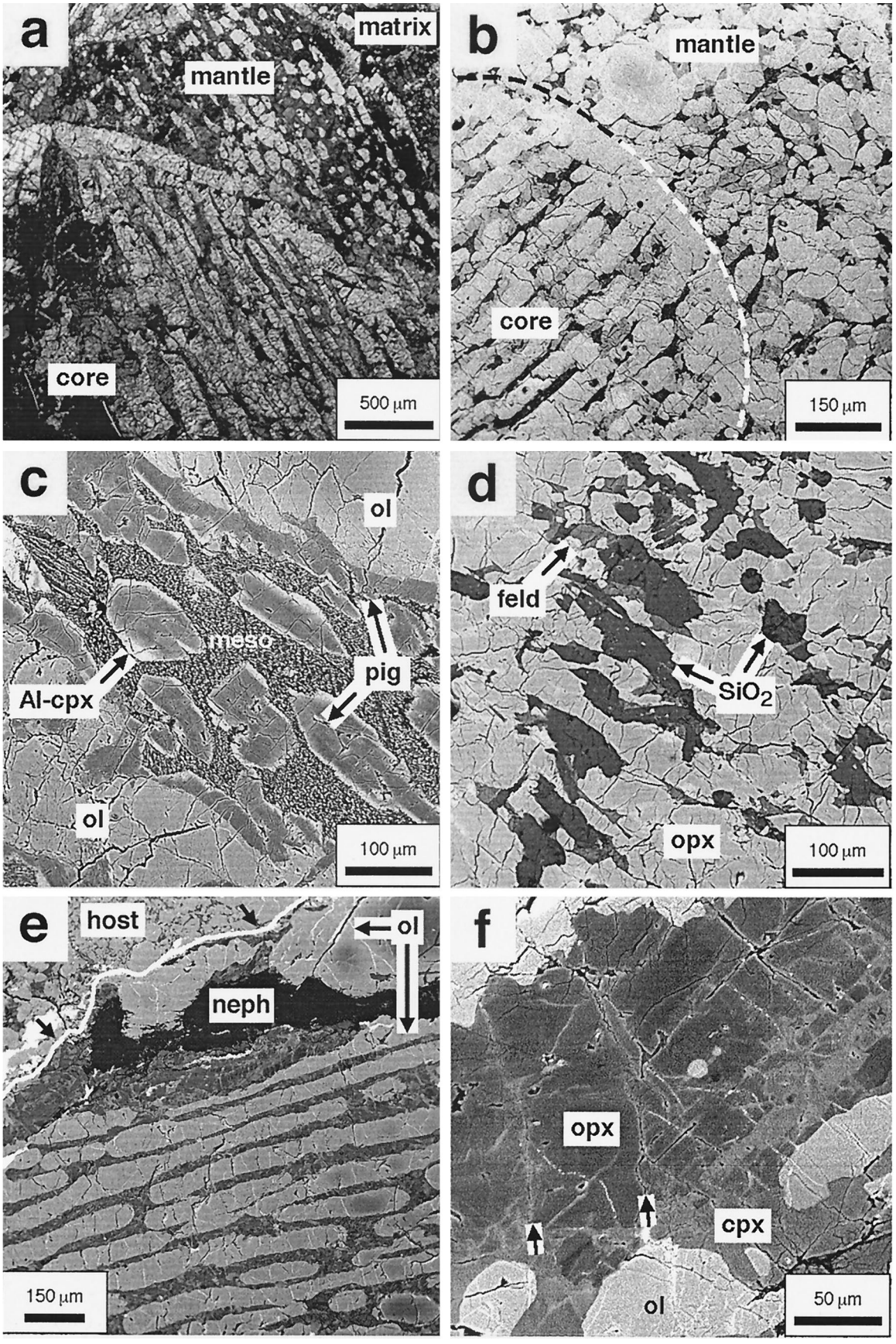
a
matrix
mantle
core
500 μm
b
mantle
core
150 μm
c
ol
meso
pig
Al-cpx
ol
100 μm
d
feld
SiO2
opx
100 μm
e
host
ol
neph
150 μm
f
opx
cpx
ol
50 μm

3.2.3. Localized shock-melting

Some clasts were locally shock-melted. Small (<200 μm-diameter) glass-rich areas within Co-1 and Gu-1 (Fig. 3a,b) appear to be typical melt-pockets (Dodd and Jarosewich, 1979, 1982) produced by localized shock-melting. These pockets are found along veins that cross-cut both the clasts and hosts (Fig. 3b), indicating that they formed during late shock events after the agglomeration of the meteorites. Regions that were locally shock-melted in Co-1 are macroscopically dark and stand out against the overall light background of the clast, providing a good example of shock-blackening (Dodd, 1981). Glassy and metal/sulfide-rich veins also cross-cut Jl-5 and Jl-16, although these veins are less conspicuous than those in Co-1 and Gu-1. Shock may have contributed to the dark appearance of clasts Gu-1, Jl-5, and Jl-16, although not all dark-colored objects (e.g., mega-chondrule Jl-17) show obvious shock-effects.

3.2.4. Inclusion Jl-7 and the large shock-melt region in Julesberg

Whereas some large melt objects experienced post-formation localized shock-melting, object Jl-7 probably formed as a shock melt. The overall texture of Jl-7 suggests that it is a clast-laden melt (Fig. 2e). The inclusion is composed of angular-to-rounded lithic and mineral clasts set within a fine-grained (≤20 μm) groundmass rich in olivine and feldspathic glass. The largest lithic clast (~1 mm across) within Jl-7 is an olivine microporphyry, and many smaller lithic clasts are of the same type (Fig. 2e). These clasts were probably derived from one or more broken chondrules that were incorporated into a melt that solidified to form the groundmass of the object. Some of the clasts within Jl-7 are barely distinguishable from the groundmass and differ only subtly in grain size and composition (Fig. 2e); these may represent debris almost completely assimilated into the melt. Most of the mineral clasts (up to ~100 μm across) consist of low-Ca pyroxene that are readily identified in BSE imaging because they are much more magnesian than the groundmass olivine.

The large shock-melt region in Julesberg 4599-1 is texturally similar to Jl-7 and consists primarily of small (≤50 μm diameter) mineral clasts (Fig. 3c), and larger (mm-sized) lithic clasts extensively veined by FeNi-metal and troilite (Fig. 3d), enclosed in a fine-grained (10 μm) groundmass. As with Jl-7, the shock-melt region contains clasts of low-Ca pyroxene that are much more magnesian than the surrounding groundmass phases. Unlike Jl-7, the melt region is rich in troilite and metal, and intergrades with the host.

3.2.5. Metamorphism

Some large melt objects in equilibrated (type 4-6) chondrites (e.g., Ho-1 in Homestead, L5; Et-1 in Etter, L5) have indistinct margins, suggesting in situ recrystallization during metamorphism of the host rock. In contrast, other large melt objects, found in both unequilibrated and equilibrated ordinary chondrites, have sharp boundaries and apparently were not significantly recrystallized in situ. These include Vi-1 (Fig. 2f) and Vi-2 in Vishnupur (LL4-6); Co-1 (Fig. 2a) in Cook (H5); and Ev-1 in Eva (H4). Similarly, Rubin et al. (1983) noted that some large melt rocks in metamorphosed chondrites showed distinct margins and that others showed indistinct margins. Possibly, some large melt inclusions were incorporated into their hosts after, and some before, metamorphism (Rubin et al., 1983).

3.2.6. Metasomatism

Petrographic study and x-ray mapping shows that several inclusions are enriched in volatile species (FeO, Na, K, P, Cl) near their margins, suggesting that they reacted with a volatile-rich external medium and were metasomatized (Table 4). Evidence for metasomatism includes the presence of feldspathoids and phosphate near inclusion margins (Fig. 1e), the presence of narrow (≤5 μm wide) FeO-enriched veinlets centered on cracks within low-Ca pyroxene (Fig. 1f), and minor compositional gradients that are oriented radially in the inclusions (Table 4).

Feldspathoids and phosphates are correlated with enrichments of Na, K, and P observed in x-ray maps. In Jl-18, feldspathoid appears to have formed by the alteration of feldspathic glass and pyroxene in the groundmass of the object (pyroxene pseudomorphs within the glass are visible). Nearby olivine phenocrysts are slightly corroded but otherwise unaffected (Fig. 1e).

FeO-enriched veinlets within low-Ca pyroxene (Fig. 1f) suggest that an influx of Fe^{2+} occurred along cracks in the objects, possibly carried by a vapor phase that could have easily penetrated into the cracks. Such veinlets have not been unequivocally identified in olivine.

Evidence for metasomatism is primarily limited to the outermost ~200 μm of the inclusions, although narrow FeO-enriched veinlets in pyroxene occur throughout most of Jl-20. This penetration depth may have important implications for normal-sized chondrules. If a similar metasomatism also affected normal-sized chondrules and was diffusion-controlled, the overall compositions of chondrules could have been sub-

Fig. 1. Micrographs of mega-chondrules obtained with cross-polarized transmitted light (a) and backscattered electrons (BSE) (b-f). (a) Ho-1. A core with barred-olivine-pyroxene texture (lower left) is separated from a mantle with barred/poikilitic texture (upper right) by a curved olivine shell. The curved margin of the mega-chondrule is visible at upper right. (b) Jl-15. A core with barred-olivine texture (lower left) is surrounded by a mantle with granular-olivine texture (upper right). Olivine = medium grey; low-Ca pyroxene = darker grey; feldspathic glass = black. (c) Jl-3. Area between olivine bars (ol, light grey) showing pigeonite (pig, dark grey), aluminous clinopyroxene (Al-cpx, light grey), and glassy mesostasis (meso, speckled). Pigeonite occurs both as individual grains and as overgrowths on the olivine; the aluminous clinopyroxene occurs on the margins of pigeonite adjacent to the mesostasis only. (d) Jl-12. Low-Ca pyroxene grains (opx, medium grey) are aligned from upper left to lower right, and interstitial glasses including Si-rich glass (SiO_2, dark-grey-to-black) and feldspathic glass (feld, dark-grey) occur in linear zones at high angles to these pyroxene grains. (e) Jl-18. This inclusion has a barred-olivine texture and a brecciated margin. Feldspathoids (neph, black) including nepheline and sodalite preferentially replace pyroxene and glass in the groundmass of the object. The arrows indicate two locations in which groundmass immediately adjacent to the host is unaltered, implying the formation of the feldspathoids prior to brecciation. (f) Jl-13. Low-Ca pyroxene (opx) contains narrow veinlets of Fe-enriched pyroxene (lighter grey) along cracks (arrows). The Fe-enriched veinlets appear similar to diopsidic pyroxene (cpx) in this image.

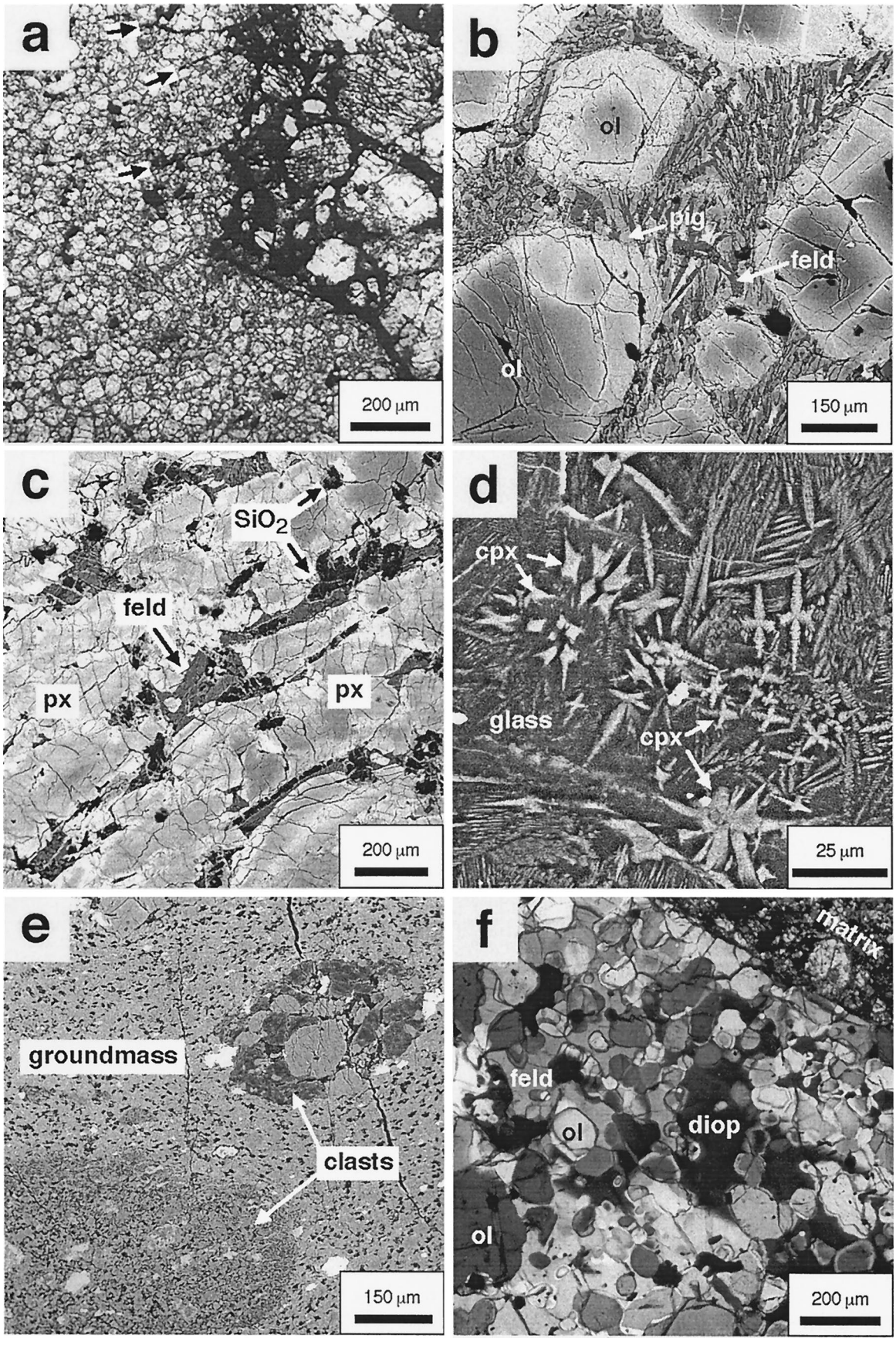
a
200 μm
b
ol
pig
feld
ol
150 μm
c
SiO_2
feld
px
px
200 μm
d
cpx
glass
cpx
25 μm
e
groundmass
clasts
150 μm
f
matrix
feld
ol
diop
ol
200 μm

stantially affected by metasomatism. Metasomatic effects are more apparent in Na-poor inclusions than in Na-rich inclusions. Of the nine inclusions showing evidence for metasomatism (Table 4), all but one (Vi-1) are Na-poor.

Close examination of mega-chondrules Jl-13 and Jl-18 reveals that feldspathoids are not always present at the margins of the objects, where they might be expected if they formed by in situ reaction with the host (Fig. 1e). Similarly, FeO-enriched veinlets are not always present in pyroxene grains close to inclusion margins despite being present elsewhere in the same inclusions. This suggests that at least some of the volatile-element influx experienced by large inclusions occurred prior to brecciation. On the other hand, the tendency for metasomatic effects to occur along brecciated margins in lithic clasts such as Jl-4, Jl-6, Jl-11, and Vi-1 imply that these objects were metasomatized after brecciation. Evidently, volatile-element addition occurred both before and after brecciation in different objects.

3.3. Phase Compositions

Mean compositions for olivine, pyroxene, and feldspathic phases in large melt inclusions are given in Table 3 and Fig. 4, and representative analyses for these phases and for Cr-spinel are given in Table 5.

3.3.1. Feldspar and feldspathic glass

Plagioclase and feldspathic glass have drastically different compositions in different inclusions (Table 3). The compositions fall mainly into two groups (Fig. 4), and this can be used to classify the objects into two different chemical types (Table 2). Sodium-poor inclusions generally contain relatively calcic plagioclase or feldspathic glass ($An_{40\text{-}95}$, with compositions of $\sim An_{70\text{-}90}$ most common) (Fig. 4, Table 3). In contrast, Na-rich inclusions contain relatively sodic plagioclase or feldspathic glass ($\sim An_{2\text{-}25}$; Fig. 4, Table 3). The distinction between Na-poor and Na-rich is not dependent on whether the analyzed phase is feldspathic glass or feldspar, as both groups contain representatives of each phase (Table 5a). Moreover, there is no obvious systematic difference in An content between the feldspar and glass in objects that contain both of these phases (Table 3).

Plagioclase and feldspathic glass of the Na-rich group is similar in composition to that found in highly equilibrated (type 6) ordinary chondrites, while that in the Na-poor group is much more calcic (Fig. 3). This implies that the feldspathic phases in Na-rich objects could have equilibrated with ordinary chondrite material, but that the same is not true for the Na-poor objects.

Mega-chondrule Ho-1 contains the most sodic plagioclase ($An_{40\text{-}70}$) of the Na-poor group (Fig. 4, Table 3). This relatively sodic composition may have been the result of partial metamorphic exchange with the surrounding host, as suggested by the textural evidence for in situ metamorphism of this object (see above). However, it is notable that Ho-1, which was apparently metamorphosed to type 5 grade, still has a feldspar composition distinct from that found in equilibrated (type 6) chondrites (Fig. 4). Evidently, the composition of feldspar in large melt inclusions was relatively resistant to metamorphism-induced re-equilibration.

3.3.2. Olivine

In contrast to feldspathic phases, olivine grains in most melt objects in this study are rather uniform in composition (typically $Fa_{18\text{-}25}$) (Fig. 4, Table 3). The olivine grains have low CaO contents (typically 0.10–0.15 wt%; Table 5a). Both the Fa and CaO content of the olivine are similar to that found in equilibrated H- and L-chondrites (Dodd, 1981). Inclusion Vi-1 contains olivine with a composition appropriate to that of an LL4-6 chondrite (Fig. 4), similar to the host. These data suggest that much of the olivine in the large melt objects could have equilibrated with ordinary chondrite material similar to the hosts in which they are found. Some inclusions (notably Jl-1 and Jl-9) have normally zoned grains with forsteritic cores ($Fa_{9\text{-}13}$) and more fayalitic rims ($Fa_{22\text{-}23}$) (Table 5a), consistent with fractional crystallization.

3.3.3. Pyroxene

Large melt objects contain a variety of pyroxene types (Table 3, 5a). In most objects, low-Ca pyroxene (with $\leq Wo_{20}$) consisting of orthopyroxene (pyroxene with the orthoenstatite or clinoenstatite structures) or pigeonite predominates, although in mega-chondrule Jl-13 and clast Vi-1, diopside is prevalent. Often, pigeonite mantles orthopyroxene, or occurs as individual grains in the mesostases of the objects. In mega-chondrules Jl-3 and Ho-1, an aluminous clinopyroxene mantles pigeonite and occurs at the interface between pigeonite and the feldspathic mesostasis (Fig. 1c). This Al-clinopyroxene contains up to 12 wt% Al_2O_3 in Jl-3 and 6 wt% in Ho-1 (Table 5a). Aluminum in these pyroxenes appears to be largely incorporated as a Ca-Tschermak component ($CaAl_2SiO_6$). In Jl-3, the Al-clinopyroxene has well-formed crystal faces where it projects into the glassy mesostasis (Fig. 1c), which suggests growth at the expense of the mesostasis (or the melt that this mesostasis represents).

In most objects, pyroxene minerals are zoned, either concen-

Fig. 2. Micrographs of large lithic clasts obtained with plane-polarized transmitted light (a), BSE (b-e), and cross-polarized transmitted light (f). (a) Co-1 in Cook (H5). The 8-mm-diameter clast is an olivine microporphyry that has an irregular margin against the host (at right, with chondrules). Thin shock-melt veins (black, arrows) penetrate into the clast from the host. (b) Jl-1. Large, normally zoned olivine grains (ol) are set in a groundmass containing pigeonite (pig, medium-to-light grey) and bytownite (feld, dark grey) laths. (c) Jl-10. Typical texture showing normally-zoned low-Ca pyroxene (px, medium grey) with interstitial tridymite (SiO_2, black) and bytownite (feld, dark grey). (d) Jl-5. Close-up of the mesostasis which contains abundant, sodic glass (dark grey) and numerous crystallites of clinopyroxene (cpx, light grey). The crystallites have distinctive dendritic and cross-shaped morphologies suggestive of rapid cooling. (e) Jl-7. The inclusion contains various clasts (including an olivine microporphyry clast at upper right, and a fine-grained ghost clast at lower left) set within a fine-grained, spongy groundmass containing feldspathic glass (tiny dark spots) and olivine (medium grey). Metal and occasional Cr-spinel and troilite grains (white) are sprinkled throughout. (f) Vi-1. The clast has a relatively coarse-grained, holocrystalline, poikilitic texture composed of olivine (ol) enclosed by oligoclase (feld) and diopside (diop). The margin of the clast (upper right) is well-delineated.

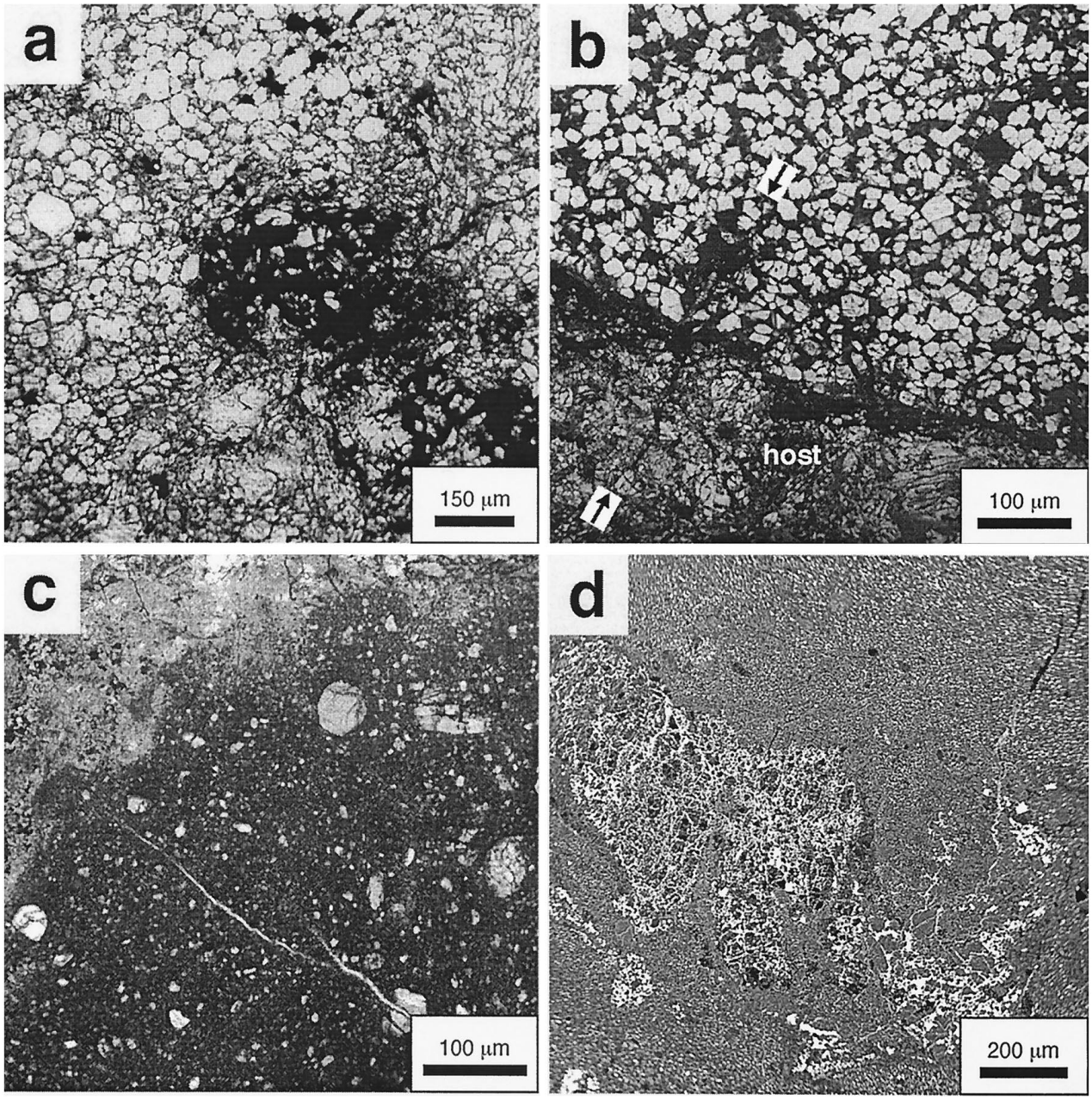

Fig. 3. Micrographs of shock-melt features in large melt inclusions and their hosts, obtained in transmitted plane-polarized light (a, b, c) and BSE (d). (a) Melt-pocket within clast Co-1, an olivine microporphyry. The glassy melt-pocket (at center) is rounded and contains insets of olivine (light grains). (b) Shock-melt veins occurring within and around clast Gu-1 (olivine microporphyry at top) and the host (at bottom). The clast is entirely surrounded by a shock-melt vein (dark region at contact with host). Some veins (arrows) appear to cross-cut both the clast and host and lead to melt-pockets within Gu-1. (c) Large shock-melt region within Julesberg AMNH 4599-1. The dark region contains mineral clasts set within a glassy groundmass containing numerous minute metal and sulfide grains; the lighter region at upper left contains relict chondrules set within glass that contains less metal and sulfide. (d) Large shock-melt region within Julesberg 4599-1, showing a deformed and veined chondrule engulfed in the glassy groundmass of the melt region. Metal and troilite (white) occur as veins within the chondrule and as tiny grains (tiny white spots) within the melt groundmass.

trically within individual grains (Fig. 2c), or asymmetrically from apparent nucleation sites on olivine towards feldspathic mesostases (Fig. 1c). During pyroxene crystallization, incompatible or moderately compatible elements (Ti, Al, Ca, Fe, Na) were enriched and compatible elements (Mg, Cr) were depleted, as expected for igneous crystallization. This pattern is shown in (1) the core-to-rim zoning of individual mesostasis pigeonite grains (e.g., Jl-3), and in the chemical differences between (2) coarser low-Ca pyroxene and finer-grained (mesostasis) pigeonite (e.g., Jl-10), and between (3) pigeonite or low-Ca pyroxene grain cores and Al-clinopyroxene (Table 5a). Thus, pyroxene zoning patterns in large melt objects provide

Table 4. Large melt objects showing evidence for metasomatism.

object	type of metasomatism	effect
Jl-4	Na influx	formation of nepheline
Jl-6	Na, Fe^{2+} influx	minor compositional gradients
Jl-11	Na, K, P influx	formation of nepheline, phosphate
Jl-13	Na, K, P, Fe^{2+} influx	formation of nepheline and phosphate in rim layer; FeO-enrichment along cracks in pyroxene
Jl-16	K influx	K-bearing veinlets
Jl-18	Na, K, Cl, P influx	formation of nepheline, sodalite, phosphate; K-bearing veinlets
Jl-19	Fe^{2+} influx	FeO-enrichment along cracks in pyroxene
Jl-20	Fe^{2+} influx	FeO-enrichment along cracks in pyroxene; probable FeO-enrichment of olivine
Vi-1	Na influx	minor compositional gradient in feldspar

good evidence that the objects crystallized from melts that were experiencing fractional crystallization. The Al-clinopyroxene in Jl-3 and Ho-1 appears to have been the last pyroxene to crystallize, just before feldspar crystallized from the residual melt. Rapid cooling may have delayed the crystallization of feldspar in these objects, resulting in the especially high Al content of the pyroxene.

Low-Ca pyroxene (orthopyroxene, pigeonite) grains in large melt objects have more varied compositions than those for olivine (Fig. 4, Table 3). Experimental data for olivine and low-Ca pyroxene pairs under metamorphic and igneous conditions (Medaris, 1969; Jones, 1995) suggest that these minerals are out of equilibrium in at least six inclusions (Jl-7, Jl-9, Jl-13, Jl-14, Jl-18, Jl-19). These six inclusions are those with the lowest Fs contents in low-Ca pyroxene (Fig. 4). This disequilibrium probably reflects preferential re-equilibration of olivine compared to low-Ca pyroxene during metamorphism or metasomatism in an FeO-rich environment (see above). Such preferential equilibration is consistent with (1) slower rates of Fe-Mg interdiffusion in pyroxene compared to olivine (e.g., Misener, 1974; Ganguly and Tazzoli, 1994), (2) more pronounced igneous zoning patterns in pyroxene, and (3) the observation that FeO-enriched veinlets occur in low-Ca pyroxene only, and not in olivine, which would arise if diffusion had gone to completion in olivine but not pyroxene.

While olivine grains in the large melt objects may have largely equilibrated with their surroundings at lower temperatures, the same does not appear to have been true for pyroxene, which preserved much of its igneous zoning.

3.3.4. Cr-spinel

Cr-spinel in large melt objects is compositionally distinct from the chromite typically found in ordinary chondrites. The analyzed grains have lower Fe/[Fe+Mg] (~0.4–0.8) and Cr/[Cr+Al] ratios (~0.1–0.7) and lower V_2O_3 concentrations (~0.10–0.50 wt%) than those found in ordinary chondrites (Table 5b). Titanium and zinc contents of the Cr-spinel grains vary widely (Table 4b). Graham (1993) previously noted a tendency for spinel grains in light-colored inclusions from Julesberg to have distinctive compositions, and this is supported by the data reported here.

3.4. Modal Compositions

Modal compositions for large melt inclusions are given in Table 6. The modes vary appreciably both in total feldspar or feldspathic glass abundance and in olivine/pyroxene ratio. Feldspar and feldspathic glass abundances vary from ~30 vol% in Jl-5 and Et-1 to ~5–7% in Jl-10, Jl-11, Jl-12, and Jl-20. Olivine/pyroxene ratios range from zero in Jl-10 and Jl-12 to ~10 in Jl-4 and ~32 in Jl-7. While there is no obvious difference in modes between mega-chondrules and lithic clasts, the most feldspathic objects are Na-rich, and the least feldspathic objects are Na-poor.

3.5. Bulk Compositions

Bulk compositions for large melt objects, including nineteen Na-poor and eight Na-rich inclusions, are given in Table 7. The groundmass composition of the large shock-melted region in Julesberg 4599-1 is given in Table 8.

Sodium-poor and Na-rich inclusions can be distinguished by differences in atomic Na/Al and (Na+K)/Al ratios. The Na/Al ratio in Na-poor inclusions ranges between 0.07–0.28 and is mainly <0.20, whereas the same ratio in Na-rich inclusions is between 0.46–0.85. For comparison, the Na/Al ratio in CI-chondrites is ~0.68 (Anders and Grevesse, 1989), indicating generally chondritic Na/Al values in Na-rich inclusions and subchondritic values in Na-poor inclusions. The two chemical types also differ in total alkali abundance, with all but one of the Na-poor objects having lower (Na+K)/Al ratios than the Na-rich objects (Table 7). The single exception is provided by Na-poor clast Vi-2, which has the highest K content of any object (Table 7).

3.5.1. CI-normalized abundances

The CI-normalized abundances of major-elements in large melt inclusions vary, but overlap that of ordinary chondrite silicate for most elements (Al, Ti, Ca, Mg, Si, Cr, Fe) (Fig. 5). Sodium-poor objects are generally depleted in Mn, Na, and K compared to ordinary chondrite silicate, while Na-rich objects have generally chondritic abundances of these elements (Fig. 5). As Mn, Na, and K are relatively volatile, this implies that Na-poor objects, but not Na-rich objects, were affected by vapor-fractionation. Furthermore, Fig. 5 demonstrates that there is no obvious chemical difference between mega-chondrules and lithic clasts of the same chemical group (Na-rich and Na-poor), suggesting that objects of the same chemical group formed by the melting of similar precursor materials and experienced similar geochemical processes. All of the inclusions are highly depleted in Ni and S compared to CI-chondrites (Fig. 5), owing to their low metal and sulfide abundances.

3.5.2. Bulk-chemical trends

In this section, we identify important bulk-chemical trends for the large inclusions and discuss how these trends may have originated. Key diagrams include an Na-Al plot (Fig. 6), a

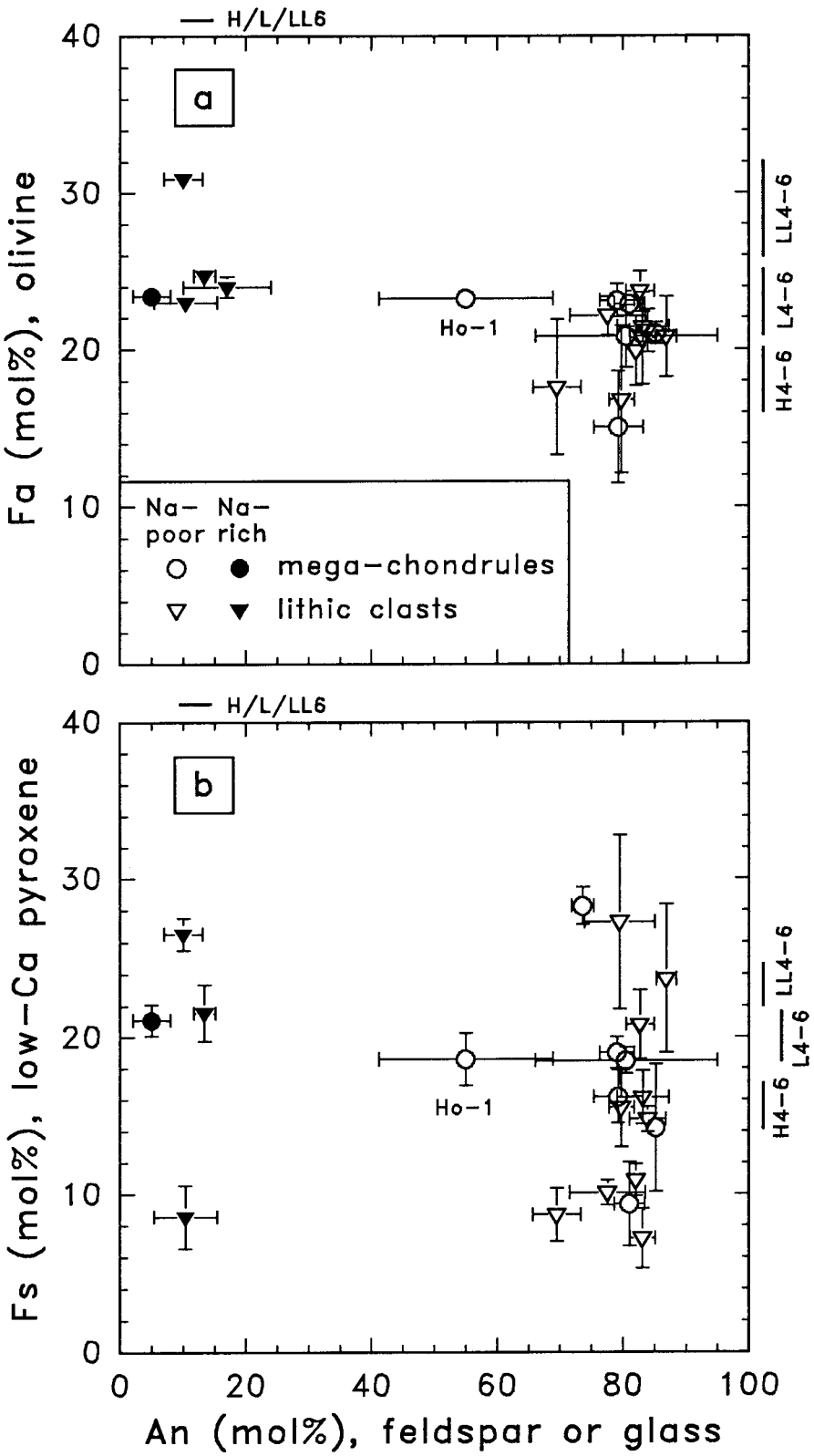

Fig. 4. Phase compositions in large melt objects (mean ± one standard deviation). (a) An = 100 · Ca/(Ca+K+Na) in plagioclase or feldspathic glass vs. Fa = 100 · Fe/(Mg+Fe) in olivine. (b) An content in plagioclase or feldspathic glass vs. Fs = 100 · Fe/(Mg+Fe+Ca) in low-Ca pyroxene. Triangles = large lithic clasts; circles = mega-chondrules; shaded symbols = Na-rich objects; unshaded symbols = Na-poor objects. Data are from Table 3, except for the composition of glass in Jl-5, which was estimated. Ranges of Fa and Fs contents in H4-6, L4-6, and LL4-6 chondrites (along right side of plots) are from Dodd (1981); the range of An contents for H6, L6 and LL6 chondrites (along top of plots) is from Van Schmus and Ribbe (1968).

Table 5a. Representative analyses of pyroxene, feldspathic phases, and olivine in large melt objects. §

	pyroxene					feldspathic phases							olivine	
	Jl-3 pig grain core	Jl-3 Al-cpx adj. glass	Ho-1 Al-cpx in meso	Jl-10 opx grain core	Jl-10 pig grain rim	Jl-2 feld	Ho-1 feld	Jl-4 feld	Jl-10 feld	Jl-3 glass	Jl-7 glass	Vi-1 feld	Jl-1 grain core	Jl-1 grain rim
wt%														
SiO_2	54.1	46.5	50.9	56.3	50.5	46.0	50.7	45.7	46.8	55.5	65.5	66.7	40.7	38.4
TiO_2	0.11	1.15	0.69	<0.03	0.40	0.05	0.04	<0.03	<0.03	0.38	0.06	0.08	n.a.	n.a.
Al_2O_3	1.62	11.7	5.83	0.23	2.08	33.9	31.2	34.2	33.0	20.3	17.8	20.5	n.a.	n.a.
Cr_2O_3	0.67	0.63	1.32	0.41	0.66	<0.03	<0.03	0.07	<0.03	<0.03	0.09	<0.03	0.12	0.04
MgO	27.7	14.9	14.7	30.7	11.3	<0.03	<0.03	<0.03	0.13	4.82	2.92	<0.03	50.2	40.6
CaO	2.01	16.2	21.8	0.46	5.27	17.6	13.9	17.5	15.7	12.6	1.63	1.42	0.03	0.03
MnO	0.34	0.31	0.20	0.19	0.47	<0.03	<0.03	0.03	0.04	0.18	<0.03	0.03	0.09	0.52
FeO	12.7	8.46	3.96	12.2	29.9	0.23	0.15	0.45	0.77	4.41	1.99	0.51	9.03	20.2
Na_2O	0.05	0.10	0.68	0.03	0.16	1.65	3.67	1.52	2.38	1.20	9.46	10.3	n.a.	n.a.
K_2O	n.a.	n.a.	n.a.	n.a.	n.a.	0.04	0.07	0.04	0.07	0.05	0.43	0.67	n.a.	n.a.
	99.30	99.95	100.08	100.22	98.74	99.48	99.73	99.46	98.91	99.43	99.88	100.22	100.17	99.79
mol%														
Wo	4.0	37.1	47.9	0.8	11.8									
En	76.0	47.3	44.9	80.8	35.2									
Fs	20.0	15.7	7.2	3.6	18.3									
An						85.3	67.5	86.2	78.1	(84.9)	(8.5)	6.8		
Or						0.2	0.4	0.2	0.4	(0.4)	(2.6)	3.8		
Ab						14.4	32.1	13.6	21.5	(14.7)	(88.9)	89.4		
Fa													9.3	22.3

§ opx = low-Ca pyroxene; pig = pigeonite; diop = diopside; cpx = clinopyroxene; meso = mesostasis; feld = plagioclase feldspar; glass = feldspathic glass. Wo = 100 Ca/[Mg+Fe+Ca], En = 100 Mg/[Mg+Fe+Ca], Fs = 100 Fe/[Mg+Fe+Ca], An = 100 Ca/[Ca+Na+K], Or = 100 K/[Ca+Na+K], Ab = 100 Na/[Ca+Na+K], Fa = 100 Mg/[Mg+Fe]. n.a. = not analyzed.

ternary diagram involving major, nonvolatile elements (Fig. 7), and plots of important element ratios (Fig. 8).

An Na-Al diagram (Fig. 6) is useful for discriminating Na-rich and Na-poor inclusions and for interpreting how these objects formed. Sodium is a volatile element and will be readily lost in high-temperature processes, whereas Al is a refractory element and will be concentrated in high-temperature residues or condensates. As previously noted, Na-rich objects have Na/Al ratios that vary around a chondritic value, whereas Na-poor objects have subchondritic Na/Al ratios (Fig. 6).

Although Na-rich objects have generally chondritic Na/Al ratios, their abundances of Na and Al vary from generally chondritic to higher values (Fig. 6a). The compositions of Na-rich inclusions overlap that of melt-pocket glasses in ordinary chondrites and the large shock-melt in Julesberg (Fig. 6a). This is an indication that Na-rich inclusions may have formed by the shock-melting of chondritic material, in a process analogous to that which produced melt-pocket glasses and other shock-melts.

Most Na-poor inclusions define a well-defined trend in which Na and Al also co-vary, but at a much lower Na/Al ratio than for Na-rich objects (Fig. 6b). Some objects (Ho-1, Jl-11, Jl-18, Bo-1) lie off the main trend at higher Na contents. The latter displacement may have been caused by an influx of Na in these objects, caused either by partial metamorphic equilibration with chondritic hosts (as previously suggested for Ho-1) or by some other metasomatic process (as noted for Jl-18 and Jl-11; Table 4).

Although the low Na/Al ratios of Na-poor objects are consistent with vapor-fractionation (see above), the co-variation of Na and Al (Fig. 6b) is inconsistent with vapor-fractionation alone. For reference, Fig. 6b shows the compositional trends

Table 5b. Representative analyses of spinel in large melt objects, compared to the composition of chromite in L3 and H3 chondrites.

	Na-poor mega-chondrules			Na-rich clasts			
	Jl-2	Jl-15	Jl-13 rim	Jl-5	Jl-7	mean L3[§]	mean H3[§]
wt%							
SiO_2	0.15	0.13	0.15	0.17	0.08	----	----
TiO_2	0.52	0.97	0.67	0.72	0.07	0.41	1.47
Al_2O_3	23.6	21.3	56.0	13.7	57.1	3.2	3.9
V_2O_3	0.29	0.47	0.24	0.17	0.19	0.60	0.70
Cr_2O_3	42.3	43.2	7.58	51.9	7.59	61.9	60.8
MgO	5.85	4.81	13.4	3.32	13.6	2.59	2.32
MnO	0.38	0.51	0.23	0.56	0.21	0.58	0.79
FeO*	25.8	27.7	17.6	29.0	17.2	30.8	30.5
ZnO	0.75	0.60	2.33	0.64	2.38	----	----
	99.64	99.69	98.2	100.18	98.42	100.08	100.48
atom ratios[†]							
X_{Fe}	0.71	0.77	0.43	0.83	0.42	0.88	0.88
Y_{Cr}	0.55	0.58	0.08	0.72	0.08	0.93	0.91

* All Fe as FeO. † X_{Fe} = Fe/[Mg+Fe]; Y_{Cr} = Cr/[Cr+Al].
§ Bunch et al. (1967)

Table 6a. Modes (vol%) of mega-chondrules. §

	Na-poor								Na-rich
	Jl-2	Jl-3	Jl-9	Jl-12	Jl-13	Jl-15	Jl-18	Ho-1	Jl-17
ol	44.2	39.9	62.7	<0.1	55.8	74.5	56.4	39.3	12.6
opx	36.9	30.6	3.1	81.6	2.8	0.21	<0.1	44.5	<0.1
pig	7.6	2.9	14.1	4.8	4.3	14.2	16.2	<0.1	64.8
cpx	<0.1	8.2	4.0	<0.1	19.5	<0.1	4.1	3.8	1.8
plag	10.9	<0.1	15.8	<0.1	11.4	<0.1	1.5	11.3	<0.1
kfeld	<0.1	<0.1	<0.1	<0.1	<0.1	<0.1	<0.1	<0.1	<0.1
glass	<0.1	18.1	<0.1	4.0	5.1	10.1	19.6	<0.1	19.2
trid	<0.1	<0.1	<0.1	9.2	<0.1	<0.1	<0.1	<0.1	<0.1
Cr-sp	0.26	0.19	0.32	<0.1	0.77	0.74	0.83	0.97	0.76
ilm	0.13	0.10	<0.1	<0.1	0.21	<0.1	0.11	<0.1	<0.1
phos	<0.1	<0.1	<0.1	0.22	<0.1	<0.1	0.17	<0.1	<0.1
neph	<0.1	<0.1	<0.1	<0.1	<0.1	<0.1	1.1	<0.1	0.66
metal	<0.1	<0.1	<0.1	0.11	<0.1	<0.1	<0.1	<0.1	<0.1
troi	<0.1	<0.1	<0.1	<0.1	<0.1	<0.1	<0.1	<0.1	<0.1

§ ol = olivine; opx = low-Ca pyroxene (<Wo 5); pig = pigeonite (Wo 5-20); cpx = augite or diopside (>Wo 20); plag = plagioclase; kfeld = potassic feldspar; glass = feldspathic glass; trid = tridymite or other SiO_2 phase; Cr-sp = Cr-bearing spinel; ilm = ilmenite; phos = phosphate; neph = nepheline or sodalite; metal = FeNi-metal; troi = troilite.

Table 6b. Modes (vol%) of large lithic clasts. §

	Na-poor									Na-rich			
	Jl-1	Jl-4	Jl-6	Jl-10	Jl-11	Jl-14	Jl-16	Jl-19	Jl-20	Jl-5	Jl-7†	Et-1	Vi-1
ol	73.3	80.6	44.6	<0.1	67.1	79.1	63.1	59.2	4.1	36.9	82.8	32.8	53.0
opx	4.2	1.7	34.0	81.0	20.1	<0.1	<0.1	6.6	81.0	<0.1	0.38	23.6	1.26
pig	6.1	6.6	6.6	4.3	3.9	13.1	17.2	13.2	7.2	<0.1	2.2	<0.1	<0.1
cpx	<0.1	<0.1	5.2	<0.1	<0.1	<0.1	5.8	3.2	0.66	26.6	<0.1	5.0	31.6
plag	15.0	10.7	8.0	5.9	<0.1	4.2	10.6	16.2	2.6	<0.1	<0.1	25.4	12.2
kfeld	<0.1	<0.1	<0.1	<0.1	<0.1	<0.1	<0.1	<0.1	<0.1	<0.1	<0.1	4.4	<0.1
glass	<0.1	<0.1	<0.1	<0.1	5.4	3.0	1.5	<0.1	3.9	30.8	12.9	<0.1	<0.1
trid	<0.1	<0.1	<0.1	8.4	<0.1	<0.1	<0.1	<0.1	<0.1	<0.1	<0.1	<0.1	<0.1
Cr-sp	0.63	0.40	1.2	<0.1	0.81	0.47	0.78	1.2	0.16	4.8	0.20	1.2	0.28
ilm	0.24	<0.1	<0.1	<0.1	<0.1	<0.1	0.14	<0.1	<0.1	n.a.	<0.1	<0.1	<0.1
phos	0.57	<0.1	<0.1	<0.1	0.88	<0.1	<0.1	<0.1	0.30	<0.1	0.26	7.3	<0.1
neph	<0.1	<0.1	<0.1	<0.1	1.8	<0.1	<0.1	<0.1	<0.1	<0.1	<0.1	<0.1	<0.1
metal	<0.1	<0.1	<0.1	0.15	<0.1	<0.1	0.75	0.24	<0.1	0.8	1.3	0.27	0.43
troi	<0.1	<0.1	<0.1	0.21	<0.1	<0.1	<0.1	<0.1	<0.1	n.a.	<0.1	<0.1	1.3

§ n.a. = not analyzed; other symbols as in Table 6a. † Excludes lithic clasts within object.

expected for equilibrium vaporization residues (or equilibrium condensates) in a bulk system with solar or CI-chondrite-like composition, at a nominal nebular pressure of 10^{-5} bar (Wood and Morfill, 1988). A series of vaporization residues (or condensates) produced by vapor-fractionation at various temperatures would produce either a vertical trend with variable Na and chondritic Al abundances (by heating to temperatures at which not all Na was lost), or a horizontal trend with negligible Na and superchondritic Al abundances (by heating to higher temperatures) (Fig. 6b). The trend actually shown by Na-poor inclusions is different, suggesting that Na-poor objects experienced a more complex geochemical history than expected for simple vaporization or condensation.

The abundances of the principal non-volatile major-elements CaO, Al_2O_3, MgO, and SiO_2 in the inclusions should be relatively insensitive to minor compositional changes arising through processes involving metamorphic equilibration or alkali- and Fe-metasomatism. Figure 7 shows that Na-rich and Na-poor inclusions form different chemical trends in terms of these nonvolatile elements, supporting the existence of two chemical groups on a basis other than volatile-element abundances.

Sodium-rich objects form a relatively well-defined trend in Fig. 7. This trend primarily reflects variation in the abundance of normative feldspar (Ab_{100-80}) relative to a chondritic mixture of olivine (Fo_{100-70}) and pyroxene (En_{100-70}) (Fig. 7). The trend shown by large, Na-rich inclusions is once again similar to that shown by melt-pocket glasses (Fig. 7), supporting the idea that Na-rich inclusions formed by shock-melting.

Sodium-poor objects show a different, less well-defined trend, which cannot be explained by varying the abundance of any one phase (feldspar, olivine, or pyroxene). As with Fig. 6b, Fig. 7 indicates the compositional trends expected for equilibrium vaporization residues or condensates in a system with

Table 7a. Bulk compositions of mega-chondrules, reconstructed from modes and phase compositions.

	Na-poor								Na-rich	
	Jl-2	Jl-3	Jl-9	Jl-12	Jl-13	Jl-15	Jl-18	Ho-1	Jl-17	Ca-1§
wt%										
SiO_2	46.7	47.5	43.7	57	43.4	41.0	42.9	47.5	52.4	45.1
TiO_2	0.16	0.29	0.17	0.06	0.3	0.11	0.23	0.16	0.26	0.15
Al_2O_3	4.3	5.0	6.0	2.0	6.8	3.9	8.4	4.2	7.0	3.9
Cr_2O_3	0.5	0.47	0.45	0.47	0.36	0.20	0.76	0.88	1.0	0.66
FeO	13	13.6	10	15.8	12.8	17.7	12	14.1	11.8	17.9
MnO	0.27	0.34	0.24	0.22	0.28	0.38	0.22	0.37	0.39	0.46
MgO	32	28.5	35	21.3	29.1	33.7	30	29.3	22.4	26.8
CaO	2.9	3.9	4	2.4	7	2.6	5.2	2.9	2.5	2.63
Na_2O	0.19	0.4	0.40	0.20	0.37	0.25	0.66	0.6	2.1	1.83
K_2O	<0.03	<0.03	<0.03	<0.03	<0.03	<0.03	<0.03	<0.03	0.08	0.37
P_2O_5	<0.03	<0.03	<0.03	0.10	0.04	<0.03	0.08	0.03	<0.03	<0.03
Fe	0.03	<0.03	<0.03	0.13	0.04	0.07	<0.03	<0.03	0.05	---
Ni	<0.03	<0.03	<0.03	<0.03	<0.03	<0.03	<0.03	<0.03	<0.03	---
S	<0.03	<0.03	<0.03	<0.03	<0.03	<0.03	<0.03	<0.03	<0.03	---
atomic**										
Na/Al	0.07	0.1	0.11	0.16	0.09	0.10	0.13	0.2	0.51	0.77
NK/A	0.07	0.1	0.11	0.16	0.09	0.10	0.13	0.2	0.52	0.87
Si/Al	9.2	8.0	6.1	24	5.4	8.9	4.3	9.5	6.4	10
Mg/Al	9.4	7.2	7.3	13	5.4	11	4.5	8.7	4.1	8.7
Mg/Si	1.0	0.90	1.2	0.56	1.0	1.2	1.0	0.92	0.64	0.89
Mg#	0.81	0.789	0.86	0.71	0.802	0.772	0.82	0.787	0.771	0.727

§ M.K. Weisberg, pers. comm. ** NK/A = [Na+K]/Al; Mg# = Mg/[Mg+Fe^{2+}]

Table 7b. Bulk compositions of large lithic clasts, reconstructed from modes and phase compositions.

	Na-poor											Na-rich					
	Jl-1	Jl-4	Jl-6	Jl-10	Jl-11	Jl-14	Jl-16	Jl-19	Jl-20	Bo-1[¶]	Vi-2*	Jl-5	Jl-7[†]	Et-1	Vi-1	Gu-1[§]	Ev-1[‡]
wt%																	
SiO_2	41.0	40	46.2	57	42.2	41.0	41.2	43.0	55	57.5	58.0	49	41.7	47.5	45.3	49.9	47.9
TiO_2	0.19	0.05	0.19	0.04	0.09	0.05	0.18	0.15	0.13	0.04	---	0.42	0.03	0.20	0.15	0.10	0.16
Al_2O_3	5.4	3.9	3.3	2.4	2.8	2.7	4.6	6.2	3.2	2.72	4.0	10.6	2.52	6.6	2.82	2.88	3.0
Cr_2O_3	0.55	0.37	1.1	0.5	0.68	0.5	0.71	1.02	0.7	0.47	0.4	2.6	0.3	0.83	0.57	0.48	0.6
FeO	13	17	14.6	15	17	16.6	17.2	13	6.2	11.2	15.3	12.1	17.7	11.6	17.1	9.7	13.6
MnO	0.24	0.35	0.33	0.24	0.38	0.36	0.37	0.24	0.24	0.29	---	0.28	0.40	0.28	0.32	0.37	0.41
MgO	36	36	31.4	22	34	36	31.1	32	31.4	25.6	15.0	16.4	34.0	20.7	23.9	34.1	31.1
CaO	3.3	2.5	2.8	1.7	1.9	2.1	3.4	4.3	2.8	1.64	3.3	3.6	0.6	5.4	6.6	1.53	2.4
Na_2O	0.38	0.21	0.18	0.20	0.48	0.22	0.25	0.34	0.28	0.47	0.3	4.4	1.22	3.1	1.45	0.81	1.0
K_2O	<0.03	<0.03	<0.03	<0.03	<0.03	<0.03	<0.03	<0.03	<0.03	0.07	3.5	0.29	0.07	0.23	0.06	0.09	0.20
P_2O_5	0.28	<0.03	<0.03	<0.03	0.41	0.43	<0.03	<0.03	0.14	<0.03	---	<0.03	0.12	3.41	<0.03	0.19	<0.03
Fe	<0.03	<0.03	0.08	0.27	0.08	<0.03	0.72	0.23	0.11	---	---	0.69	0.9	0.25	1.2	---	---
Ni	<0.03	<0.03	<0.03	<0.03	<0.03	<0.03	0.11	0.03	<0.03	---	---	0.11	0.4	<0.03	0.03	---	0.06
S	<0.03	<0.03	<0.03	0.08	<0.03	<0.03	<0.03	<0.03	<0.03	---	---	<0.03	<0.03	<0.03	0.46	---	0.2
atomic**																	
Na/Al	0.12	0.09	0.09	0.14	0.28	0.14	0.09	0.09	0.15	0.28	0.1	0.68	0.796	0.77	0.845	0.46	0.55
NK/A	0.12	0.09	0.09	0.14	0.28	0.14	0.09	0.09	0.15	0.31	1.1	0.71	0.83	0.80	0.87	0.50	0.62
Si/Al	6.4	8.6	12	21	13	13	7.5	5.9	15	17.9	12	3.9	14.0	6.1	13.6	14.7	14
Mg/Al	8.4	12	12	12	15	17	8.5	6.5	12	11.9	4.7	1.95	17.1	4.0	10.7	15.0	13
Mg/Si	1.3	1.3	1.0	0.57	1.2	1.3	1.1	1.1	0.85	0.66	0.39	0.50	1.22	0.65	0.79	1.02	0.97
Mg#	0.83	0.79	0.793	0.72	0.78	0.79	0.763	0.81	0.90	0.803	0.636	0.706	0.775	0.761	0.714	0.86	0.803

[¶] Ruzicka et al. (1995). * Wlotzka et al. (1983); atypical (K-rich) Na-poor object. [†] Excludes lithic clasts within object. [§] M.K. Weisberg, pers. comm. [‡] Fodor and Keil (1976); defocussed beam analysis. ** NK/A = [Na+K]/Al; Mg# = Mg/[Mg+Fe^{2+}]

solar- or CI-like compositions. The highest-temperature residues/condensates have high CaO + Al_2O_3 , while fully condensed material will lie close to the MgO-SiO_2 join and have the composition of CI-chondrites (Fig. 7). The overall chemical trend shown by Na-poor objects is subparallel to the lowest-temperature portion of the vaporization/condensation curve, which involves variation in MgO/SiO_2 and in CaO + Al_2O_3 (Fig. 7). To a first approximation, the Na-poor inclusion trend could be produced by adding or subtracting to CI-chondrite composition a residue or condensate similar in composition to olivine-rich aggregates (OAs) in carbonaceous chondrites (Fig. 7). The most appropriate OAs may be those that are Na-poor (Fig. 6b).

Table 8. Major-element composition of a large (~2 x 1 cm) shock-melt region in Julesberg, compared to whole-rock Julesberg, average L-chondrite, average melt-pocket glasses in L-chondrites, and the average Na-rich large melt object of this study.

	Julesberg shock-melt [#]	Julesberg bulk*	average L-chondrite[§]	average melt-pocket[†]	average Na-rich large obj[‡]
wt%					
SiO_2	42.2 ± 2.8	40.6	39.72	48.5 ± 4.4	47.3 ± 3.1
TiO_2	0.1 ± 0.0	0.13	0.12	0.05 ± 0.07	0.18 ± 0.11
Al_2O_3	2.5 ± 0.7	2.07	2.25	6.2 ± 2.3	4.90 ± 2.69
Cr_2O_3	0.6 ± 0.3	0.53	0.53	0.39 ± 0.37	0.88 ± 0.68
FeO	11.3 ± 4.1	10.3	14.46	10.4 ± 3.0	13.9 ± 3.0
MnO	0.4 ± 0.1	0.34	0.34	0.44 ± 0.10	0.36 ± 0.06
MgO	27.5 ± 3	26.9	24.73	23.5 ± 4.5	26.2 ± 6.1
CaO	2.2 ± 0.6	1.74	1.85	2.1 ± 2.3	3.15 ± 1.85
Na_2O	1.3 ± 0.3	0.72	0.95	2.3 ± 1.2	1.98 ± 1.12
K_2O	0.1 ± 0.1	0.07	0.11	0.3 ± 0.2	0.17 ± 0.11
P_2O_5	---	0.20	0.22	---	0.47 ± 1.11
Fe	8.9 ± 4	12.5	10.7	3.0 ± 2.9	0.38 ± 0.44
Ni	0.9 ± 0.5	1.04	1.24	0.7 ± 0.8	0.08 ± 0.14
S	2.1 ± 1.1	2.3	2.10	---	0.09 ± 0.16
	100.1	99.44	99.32	97.88	100.07

[#] Obtained by averaging microprobe analyses of typical fine-grained matrix of the shock-melt region (omitting large clasts), allocating enough Fe to S to make stoichiometric FeS, enough Fe to Ni to make metal with an average L-chondrite Fe/Ni ratio (wt/wt) of 5.67 (Jarosewich, 1990), and all remaining Fe to FeO. The quoted error is the standard deviation of the mean. * Graham (1993). [§] Jarosewich (1990), average L-chondrite fall. [†] Dodd and Jarosewich (1982) and Dodd et al. (1982). The quoted error is the standard deviation of the mean. Fe and Ni contents are artificially low because an attempt was made to avoid metal grains during analysis. [‡] 8 objects, data from Table 7. The quoted error is the standard deviation of the mean.

Figure 8 shows inclusion compositions in terms of key element ratios. High-temperature residues/condensates will have low Na/Al, low Mg/Al, and low Si/Al, and fully condensed material will have the composition of CI-chondrites. In Fig. 8b, plagioclase and other Al-rich phases (e.g., gehlenite, $MgAl_2O_4$ spinel) plot close to the origin, and the olivine/pyroxene (i.e., Mg/Si) ratio increases from lower right to upper left. With increasing temperature, condensates and residues are at first increasingly olivine-rich, and then increasingly Al-rich (Fig. 8b). A very high-temperature residue/condensate will approach the composition of Ca-Al-rich inclusions (CAIs) (Fig. 8).

Sodium-rich objects form a quasi-linear trend in Mg/Al and Si/Al pointing away from plagioclase (plag) (dashed line in Fig. 8b), consistent with simple variation in the abundance of normative plagioclase.

In contrast, Na-poor inclusions form two trends when Mg/Al is plotted against Si/Al (solid lines in Fig. 8b), and a single trend when Na/Al is plotted against Si/Al (solid line in Fig. 8a). The two trends for Na-poor objects in Fig. 8b intersect near the composition of CI-chondrites and mirror the shape, although not the precise position, of the condensation/vaporization curve. The apparently systematic relationship between the compositions of the inclusions and the predicted vapor-fractionation curves implies that the chemical trends of Na-poor objects are somehow related to vapor-fractionation processes.

The generally subchondritic and uniform Na/Al ratios of Na-poor objects (Fig. 8a) suggest that they could have equilibrated at elevated temperatures, under conditions at

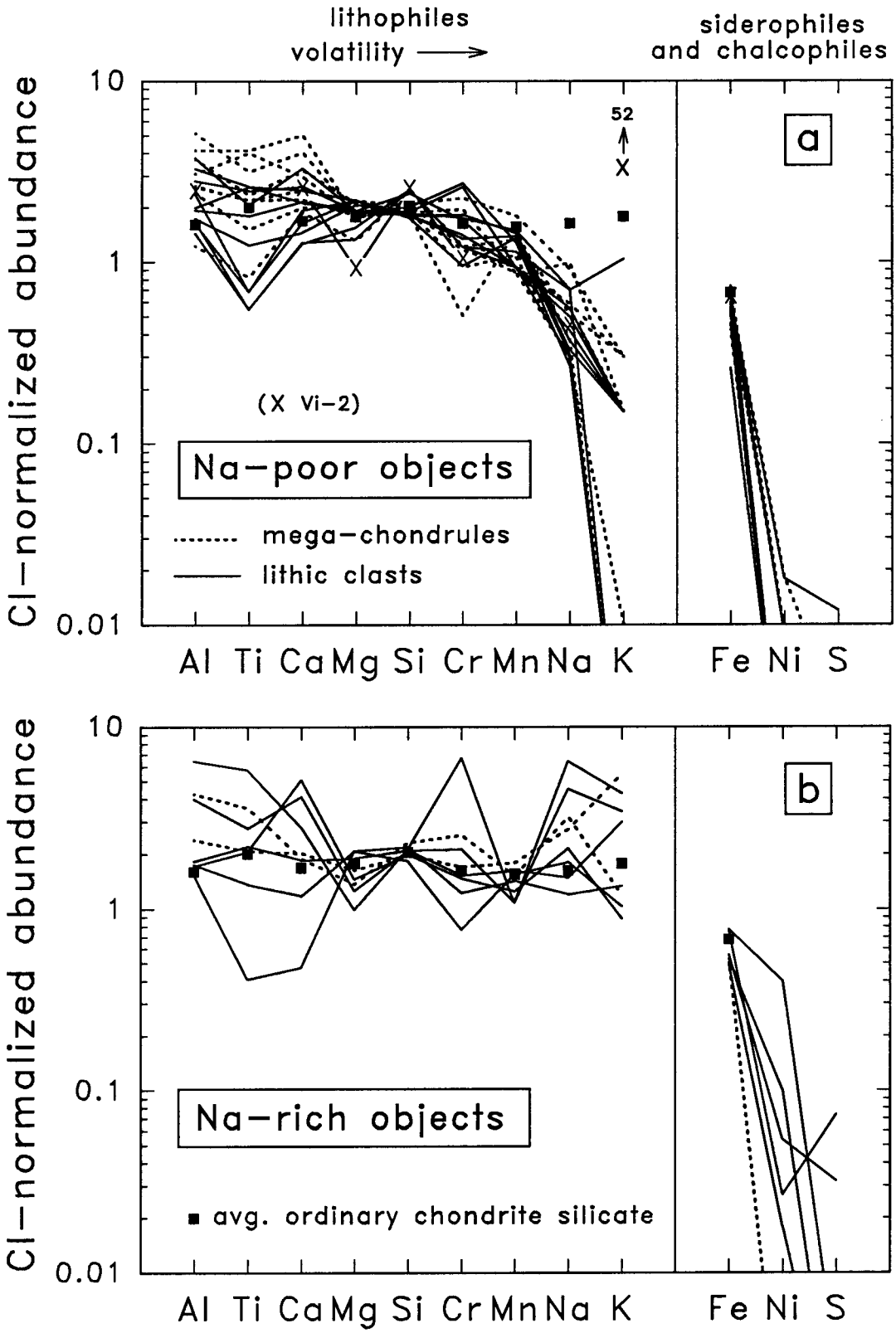

Fig. 5. CI-normalized bulk-chemical abundances in large melt inclusions. Data are from Table 7; solid lines = lithic clasts; dashed lines = mega-chondrules. Average ordinary chondrite silicate is the mean H-, L-, and LL-chondrite fall (Jarosewich, 1990) on a metal- and sulfide-free basis. The average CI-chondrite abundances of Anders and Grevesse (1989) were used for normalization.

which the atomic Na/Al ratio of the stable condensate was low (~0.1) but nonzero. However, such mild heating would leave Mg/Al and Si/Al ratios unaffected (Fig. 8). To explain variations in Mg/Al and Si/Al, it appears that the precursors of Na-poor inclusions would have had to experience vapor-fractionation at higher temperatures, under conditions in which not only Na but also Mg and Si were significantly vaporized. The uniformly low (but nonzero) Na/Al ratios of these objects could then be explained by a later re-equilibration event at a lower temperature. Modelling suggests that such equilibration could have occurred in a narrow temperature range in nebular systems in which a low-pressure gas was present (e.g., equilibration at ~1375–1450 K in a CI-like system containing gas with a pressure of 10^{-5} bar: Ruzicka et al., 1998). Consequently, the relatively uniform Na/Al ratios of Na-poor inclusions could be an indication that these inclusions equilibrated under nearly identical ambient conditions.

In detail, the two trends shown by Na-poor objects in Fig. 8b can be explained by the addition or removal of two different types of vapor condensates or residues produced at different temperatures. One trend contains Jl-4 and Jl-12 at its endpoints and is characterized by a large variation in atomic Mg/Si, ranging from ~1.8 (Jl-4) to ~0.54 (Jl-12), accompanied by a small change in Al (higher Al in Jl-4 than in Jl-12) (Fig. 8b). Jl-4 lies on the predicted residue/condensate trend and can be explained as a remelted residue/condensate that formed in a system with CI-like overall composition (Fig. 8b). More siliceous objects on the same trend, such as Jl-12, Jl-10, Jl-20, and Bo-1, could have formed by the removal of such olivine-rich material by fractional condensation or fractional vaporization in a system with CI-like composition. For fractional condensation, olivine-rich material would have been segregated from the system to leave a more Si-rich gas out of which the pyroxene-rich objects condensed. Such condensates could later have been remelted to form the Si-rich objects. For fractional vaporization, the gas evolved in the early stages of vaporization accompanying the production of an olivine-rich residue would have had low Mg/Si, and such gas could have condensed to form Si-rich material that was later remelted to form the Si-rich inclusions.

The second trend shown by Na-poor inclusions can be explained by the fractionation of an even higher-temperature condensate or residue from a system with CI-like composition. This trend is characterized by variation mainly in Al, with a fairly constant Mg/Si ratio similar to that in CI-chondrites (Fig. 8b). Aluminum-poor, sodium-poor inclusions along this trend (Jl-14, Jl-11) could have formed by the removal of an Al-rich (low-Mg/Al and low-Si/Al) residue/condensate by fractional condensation or fractional vaporization (Fig. 8b). This would occur in a manner similar to that suggested for Jl-12, Jl-10, and Bo-1, except that the fractionating residue/condensate would be more Al-rich than Jl-4, perhaps similar in composition to OAs (Fig. 8b). Aluminum-rich, sodium-poor inclusions along this trend (Jl-1, Jl-2, Jl-3, Jl-9, Jl-13, Jl-15, Jl-16, Jl-18, Jl-19, Ho-1) could have formed by the remelting of the same high-temperature residues/condensates, generally similar in composition to OAs or Al-rich OAs (Fig. 8b).

The only Na-poor inclusion that cannot be explained by these vapor-fractionation processes is the anomalous Vi-2, which has a low Mg/Si ratio, and which lies far off of the two trends shown by other Na-poor inclusions (Fig. 8b).

3.6. Origin of Large Melt Objects in Ordinary Chondrites

Large melt objects in ordinary chondrites are composed of at least two chemically distinct groups (Na-poor and Na-rich), which each contain representatives of objects that (1) solidified as independent free-floating bodies (mega-chondrules) and that (2) formed by the brecciation of even larger objects (large lithic clasts). Below, we discuss the origin of these objects.

3.6.1. Large Na-rich inclusions

Sodium-rich objects show no evidence for vapor-fractionation and are best explained as having formed by the melting of chondritic material. We suggest that these objects were produced by the complete-to-incipient shock-melting of ordinary chondrites, in a process analogous to that which formed melt-pocket glasses and large shock-melt regions in ordinary chondrites.

Sodium-rich objects with the lowest Na and Al abundances (Jl-7, Vi-1, Gu-1, and Ev-1) have roughly chondritic abundances of a feldspar component and could have formed by essentially total impact-melting of ordinary chondrite silicate. This is consistent with the interpretation of Ev-1 given previously (Fodor and Keil, 1976b), and with the textural evidence for an impact-melt origin for Jl-7 (see above).

Sodium-rich inclusions with higher normative feldspar and Na and Al abundances (Ca-1, Jl-18, Et-1, Jl-5) could have formed as impact-melts enriched in normative feldspar. Such an enrichment of feldspar in impact melts is observed in some chondrite melt-pockets (Dodd and Jarosewich, 1982) and in experimentally-produced shock-melts of basalts (Schaal and Hörz, 1977; Schaal et al., 1979). Feldspar melts at lower shock pressures than either pyroxene or olivine (Stöffler et al., 1988, 1991). Therefore, as with feldspathic melt-pockets (Dodd and Jarosewich, 1982; Dodd et al., 1982), the more feldspathic Na-rich inclusions could have formed as incipient (as opposed to total) shock melts.

The existence of unequivocal shock-melt regions in Julesberg and in other ordinary chondrites comparable in size to Na-rich inclusions shows that shock-melting of the parent bodies was able to produce melts of the required volumes, at least for the inclusions with quasi-chondritic compositions. The fact that typical melt-pockets are small ($\leq 500\mu$m across; Dodd and Jarosewich, 1979) compared to the inclusions may indicate that the pockets were constrained to fit into pore spaces within the chondrite parent body and that the same constraint did not apply to the inclusions. The shapes of Na-rich mega-chondrules suggest that they formed as freely-floating objects, perhaps produced by jetting (Kieffer, 1975) or by splashing from melt pools. Na-rich lithic clasts could have been derived by the fragmentation of even larger Na-rich mega-chondrules, or by the fragmentation of solidified melt veins or sheets.

However, recently it has been questioned whether large bodies of fractionated (relative to chondritic) compositions can be produced during shock-melting (Keil et al., 1997). The latter

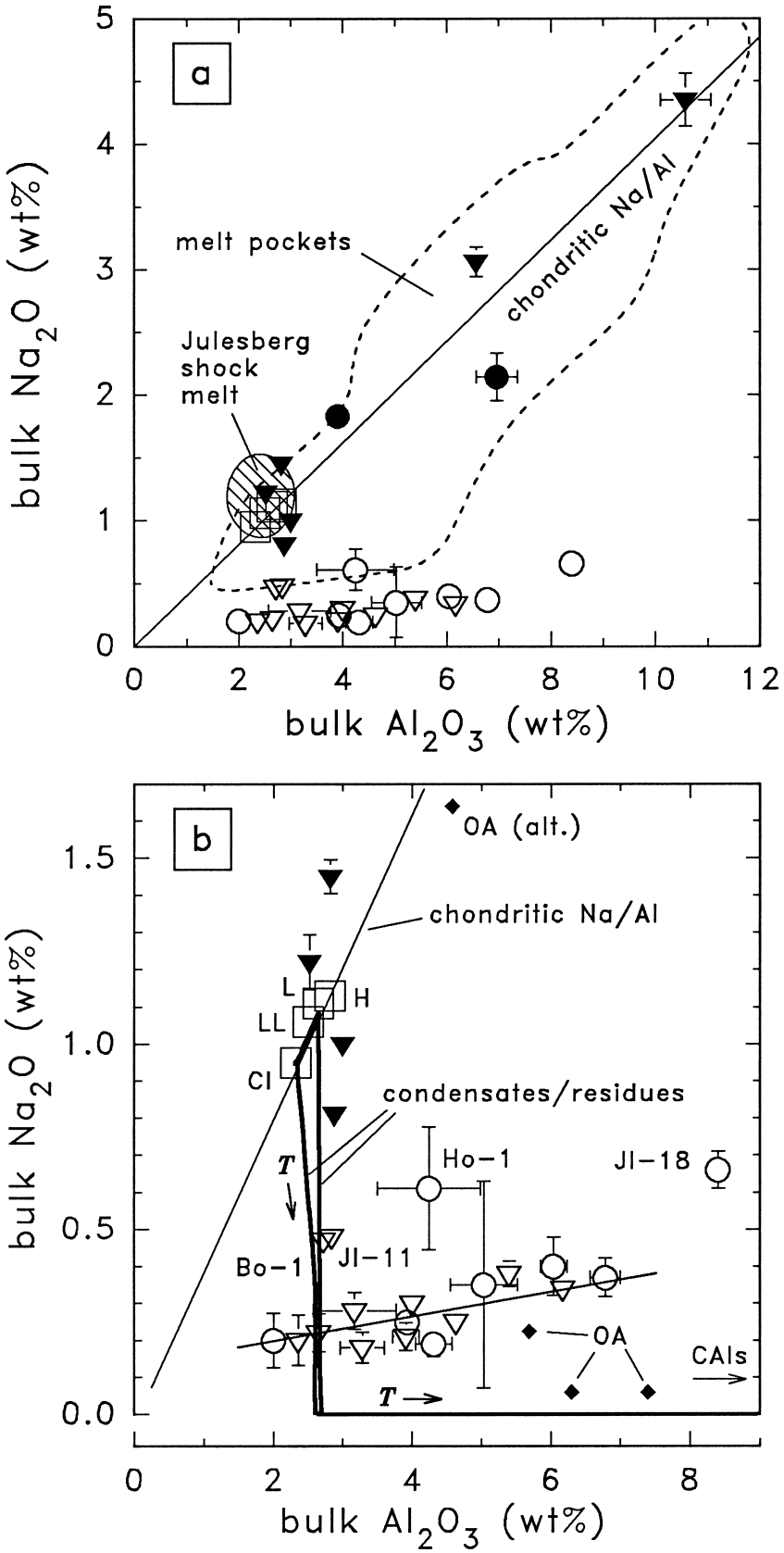

Fig. 6. Na-Al composition diagrams for large melt inclusions. The shaded region in (a) is the groundmass composition of the large shock-melt in Julesberg 4599-1. Data are from Tables 7 and 8; symbols are as in Fig. 4. Dashes in (a) show the compositional range for melt-pocket glasses in L-chondrites (Dodd and Jarosewich, 1982; Dodd et al., 1982). Bold lines

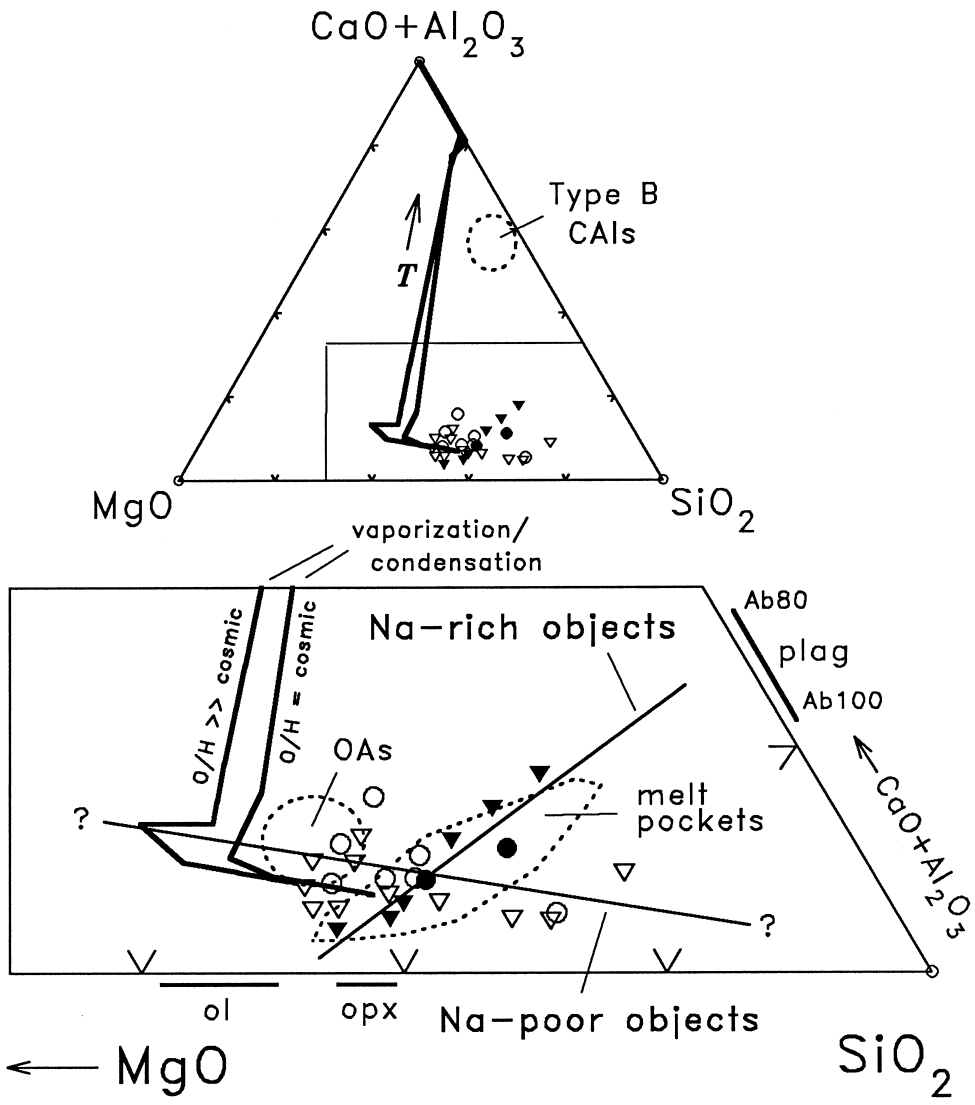

Fig. 7. Major-element compositions of large melt objects in the ternary system ($CaO + Al_2O_3$) - MgO - SiO_2. Symbols and data sources are as in Fig. 4 and 6. The compositions of representative Type B1 and B2 Ca-Al-rich inclusions (CAIs) (MacPherson et al., 1988) are shown for reference. ol = Fo_{100-70} olivine; opx = En_{100-70} orthopyroxene; plag = Ab_{100-80} plagioclase. Na-rich objects form a trend consistent with variation in the abundance of plagioclase similar to that shown by melt-pocket glasses; Na-poor objects appear to form a different trend.

authors argued that impact melts with fractionated compositions are generally microscopic, with dimensions on the scale of the target grain size. On the other hand, Rubin et al. (1986) concluded that a large (2 × 4 cm) feldspathic inclusion in the Guin IIE iron meteorite formed by incipient shock-melting of chondritic material, based on chemical comparison to ordinary chondrite melt-pockets. Thus, whether objects as large as the feldspathic Na-rich inclusions (up to a cm across) can be produced by impact-melting is unclear.

Sodium-rich objects are depleted in FeNi-metal and sulfide (Fe, Ni, and S) compared to whole-rock ordinary chondrites, the large shock-melt in Julesberg, and melt-pockets (Table 8). They could have lost most of their metal and sulfide during impact-melting. Observations of melt-pockets and the larger

in (b) show the calculated compositions of equilibrium condensates or residues at various temperatures (T) for two nebular systems (corresponding to dust/gas ratios = 1 × cosmic, and 10,000 × cosmic) containing a low-pressure gas (10^{-5} bar), derived using the PHEQ program of Wood and Hashimoto (1993). Other symbols: squares = average composition of H-, L-, and LL-chondrite falls (Jarosewich, 1990) and CI-chondrites (Anders and Grevesse, 1989); shaded small diamonds = olivine-rich aggregates (OAs), including average altered OA in Allende (OA alt.; Kornacki and Wood, 1984) and individual, relatively unaltered olivine-rich aggregates in Vigarano (Vig 1623-10; Sylvester et al., 1992) and Efremovka (Ef-8, Ef-11; Ruzicka, 1996). Sodium-rich objects form a trend similar to that of melt-pocket glasses; Na-poor objects have relatively uniform, subchondritic Na/Al ratios.

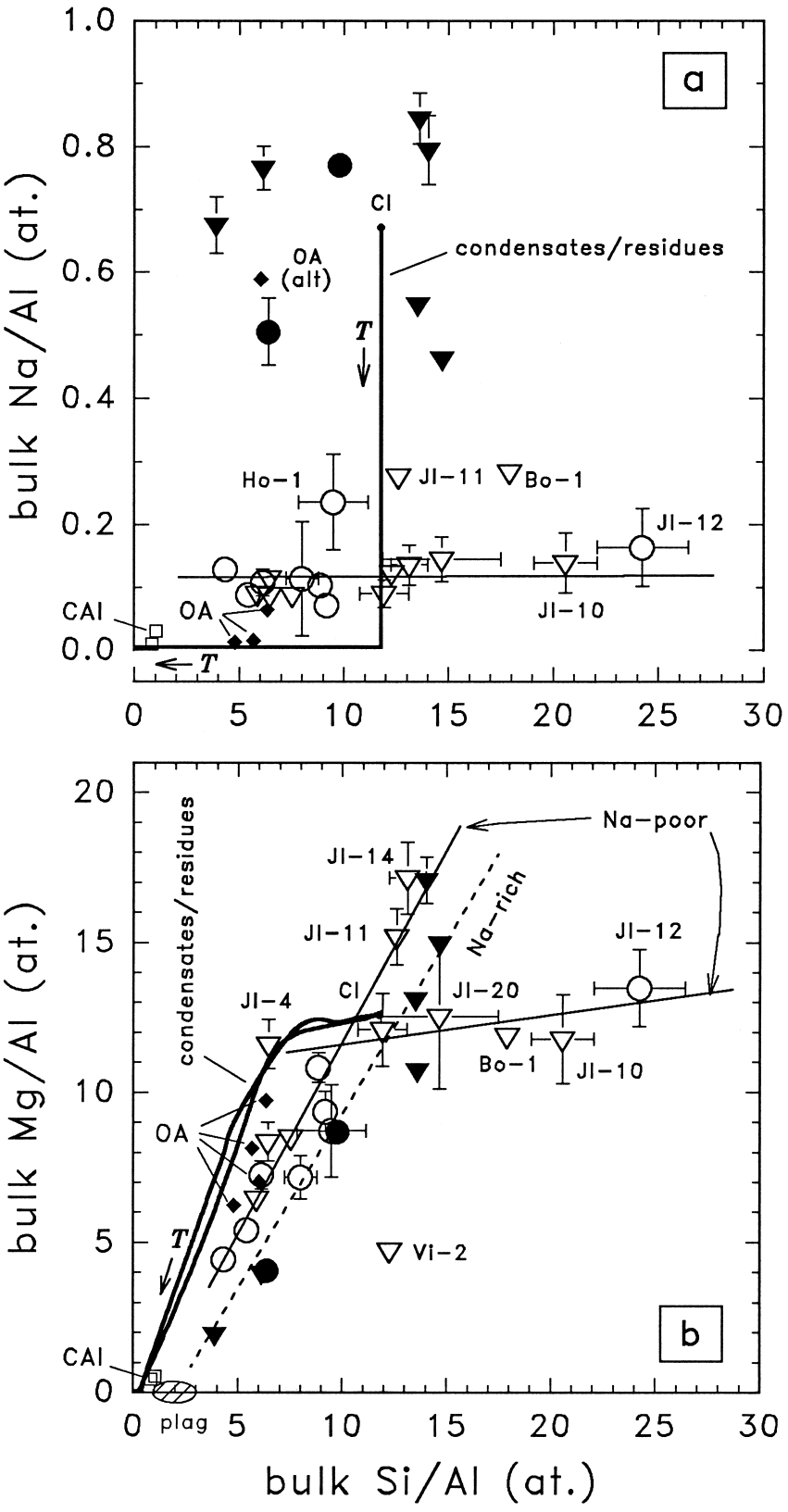

Fig. 8. Si/Al vs. (a) Na/Al and (b) Mg/Al for large melt objects. Symbols and data sources as in Fig. 4, 6, and 7. Na-rich objects show scatter in (a) but form a trend in (b) consistent with variable proportions of a feldspathic component (plag). Na-poor objects form a single trend in (a), and two trends in (b) that intersect close to the composition of CI-chondrites.

shock-melt region in Julesberg show that metal and troilite are dispersed as minute rounded blebs throughout the melts, indicative of the immiscible separation of metal and sulfide from silicate melt (Dodd and Jarosewich, 1982). In the large shock-melt region in Julesberg, these metal and sulfide inclusions are non-uniformly distributed (Fig. 3c). Moreover, relict chondrules enclosed in the shock-melt contain numerous metal and sulfide veins (Fig. 3d). These observations imply significant mobility of metal and sulfide during the shock process. Thus, the relatively low metal and sulfide abundances in Na-rich inclusions can be explained by (1) gravitational separation of metal and sulfide in a melt pool, (2) centrifugal separation of metal and sulfide in spinning melt droplets, or (3) dynamic separation during the shock-melting process itself.

3.6.2. Large Na-poor inclusions

The petrogenesis of Na-poor objects appears to have been complex, and involved (1) the formation of precursor materials that experienced vapor-fractionation processes at high temperatures; (2) a later reequilibration event at lower temperatures; (3) remelting; (4) brecciation; and (5) a late, relatively minor metasomatic influx of volatile elements (Na, K, Cl, P, Fe^{2+}).

The vapor-fractionation processes involved some combination of vaporization, condensation, fractional condensation, and fractional vaporization. These processes resulted in precursors with diverse Si/Al, Mg/Al, and Mg/Si ratios. The precursors are inferred to have included (1) relatively Al-rich (refractory) material with high Mg/Si, similar in composition to olivine-rich aggregates (OAs), (2) Al-poor (less refractory), pyroxene-rich material with low Mg/Si, and (3) Al-poor (less refractory) material with intermediate Mg/Si.

Following vapor-fractionation, the precursor materials reequilibrated with their ambient environment at a lower temperature, increasing the Na content of the interiors of the objects. Although such reequilibration would have involved a metasomatic influx of Na into the objects, it must have preceded a later metasomatism that affected only the peripheries of some of the Na-poor inclusions we now see. In a nebular system containing gas with a pressure of 10^{-5} bar, the reequilibration temperature would have been ~1375–1450 K (Ruzicka et al., 1998). This temperature is much higher than metamorphic temperatures experienced by ordinary chondrites (Dodd, 1981), clearly indicating that the reequilibration did not occur as a result of chondrite metamorphism. Judging by comparison to chondrules (Wasson, 1996), the equilibration temperature is somewhat above the solidi but below the liquidi of the inclusions. Therefore, equilibration occurred either prior to or during the last melting event experienced by the objects.

The last melting episode involved fractional crystallization as the melt solidified. Sodium-poor mega-chondrules solidified as free-floating droplets. Sodium-poor lithic clasts may have formed in a similar way, by the brecciation of even larger Na-poor droplets. Following crystallization, all of the inclusions were brecciated, and some of them interacted with a volatile-rich (Na-, K-, P-, Cl-, FeO-rich) environment in a late metasomatic episode. This late metasomatism sometimes occurred before, and sometimes after, the last brecciation event.

Sodium-poor inclusions contain very little metal and sulfide and must have formed either by the melting of metal- and sulfide-poor precursors or by the subsequent loss of these phases. The total Fe abundances in the inclusions are similar to that in ordinary chondrite silicate and lower than in bulk CI-chondrites (Fig. 5). This suggests that Fe was partitioned into metal and silicate in the inclusions in the same proportions as in ordinary chondrites. Large, Na-poor inclusions would be severely depleted in sulfide if the precursors formed at a sufficiently high ambient temperature to prevent S from condensing, as suggested by the data for Na. At first glance, it would appear that high ambient temperatures cannot also account for the dearth of metal in these objects, as metal will be stable to relatively high temperatures under the fO_2 conditions appropriate to ordinary chondrites. However, Wasson (1996) noted that metal has a shorter evaporation half-life than forsterite (and presumably other silicates), raising the possibility that the abundances of both metal and sulfide are low in Na-poor inclusions because both were selectively removed by vaporization. Thus, possible metal-silicate separation mechanisms affecting Na-poor inclusions include (1) centrifugal separation of immiscible metal in suspended droplets, (2) differential size- or mass-sorting of metal and silicate condensates in a gas-rich, possibly turbulent environment, and (3) kinetic effects that allowed metal to vaporize more readily than silicates.

The heating mechanism responsible for the vapor-fractionation and melting processes experienced by Na-poor objects is uncertain. Hypervelocity impact, inferred to have been important for producing Na-rich objects, is a possibility. A type of glass found in lunar soils and known as HASP (high-alumina, silica-poor) is inferred to have formed by impact-induced vaporization of Si relative to Al (Naney et al., 1976; Vaniman, 1990; Papike et al., 1997). Such HASP glasses are apparently concentrated in the <20 mm size fraction of lunar soils (Papike et al., 1997) and are very small; lunar HASP-like objects as large as the Na-poor inclusions have not been identified. Thus, a shock-vaporization origin for Na-poor inclusions is possible but unproven. Heating mechanisms such as those envisioned for chondrules (e.g., Boss, 1996) are also candidates for having produced large Na-poor inclusions.

3.7. Comparison to Normal-Sized Chondrules

Normal-sized chondrules in ordinary chondrites share some important similarities with large melt inclusions, making it likely that the two types of objects are related. The similarities include: (1) mineralogies dominated by olivine, low-Ca pyroxene, and a feldspathic phase; (2) textures including barred-olivine, microporphyritic olivine, radial-pyroxene, poikilitic, granular olivine, and cryptocrystalline; (3) the drop-formed character of some inclusions and chondrules; (4) the apparent existence of at least two main types of chondrules that resemble Na-rich and Na-poor large melt objects (see below), (5) chemical variations in certain lithophile elements that are consistent with vapor-fractionation processes (see below), and (6) the existence of radial gradients in Na (Ikeda and Kimura, 1985; DeHart et al., 1988; Grossman, 1996).

Normal-sized chondrules can be subdivided into Na-poor and Na-rich groups reminiscent of those found in large melt objects (Fig. 9). Ikeda (1983) studied ~200 chondrules in type 3 ordinary chondrites and found that the glass in most was relatively sodic, but that others had relatively calcic

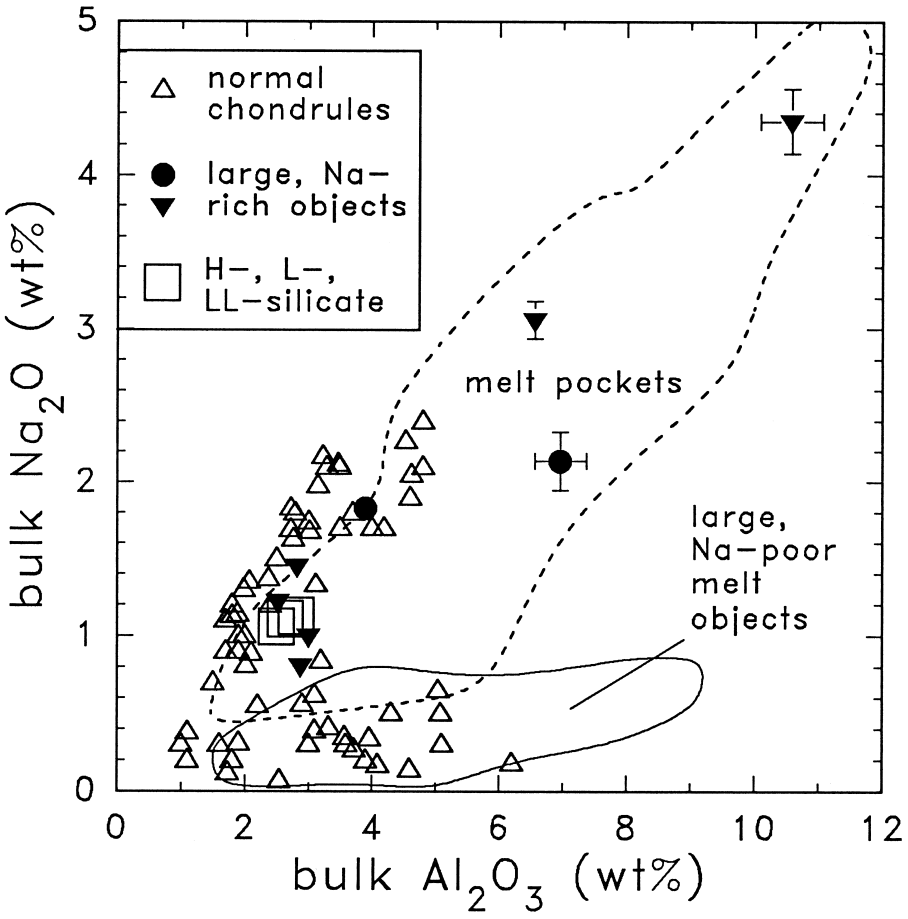

Fig. 9. Na_2O vs. Al_2O_3 diagram for normal-sized, ferromagnesian chondrules in the Semarkona LL3.0 (data: Jones and Scott, 1989; Jones 1990, 1994, 1996) and Manych LL3.5 (data: Dodd 1978a,b) chondrites, showing evidence for two trends that appear to correspond to the Na-poor and Na-rich groups of large melt objects in this study. Average ordinary chondrite silicate compositions are from Jarosewich (1990); the range of melt-pocket glass compositions are from Dodd and Jarosewich (1982) and Dodd et al. (1982).

glass. A third type of chondrule, restricted to LL-chondrites, had potassic glass. Kurat et al. (1984) analyzed chondrules in Chainpur (LL3.4) and found evidence for four types of chondrules: a refractory group that appears to correspond to the Na-poor group, a chondritic group that appears to correspond to the Na-rich group, a K-enriched group that may correspond to anomalous object Vi-2, and a K-depleted group for which there are no known obvious analogs among large melt objects. Hewins (1991) observed that type I (magnesian olivine) and type III (pyroxene-rich) chondrules mainly have atomic Na/Al < 1, whereas type II (ferroan olivine) chondrules have Na/Al ~ 1. Moreover, type II chondrules have generally chondritic abundances of major-elements, whereas type I chondrules are generally depleted in volatile-elements and enriched in refractory-elements (Hewins, 1991). This suggests that large Na-poor inclusions correspond to type I/III chondrules and large Na-rich inclusions correspond to type II chondrules.

Hewins (1991) concluded that the Na/Al ratios of type I chondrules were significantly affected by metamorphic equilibration in meteorites with subtypes of 3.6 or higher. Similarly, De Hart et al. (1992) and Sears et al. (1996) found that most chondrules in weakly-metamorphosed (subtype <3.6) ordinary chondrites have relatively calcic, feldspathic mesostases (An_{50}), with the proportion of chondrules containing more sodic mesostases increasing with petrographic subtype. Such metamorphic equilibration does not appear to have significantly affected most of the large melt objects, possibly because their large sizes (low surface-area/volume ratios) made diffusive exchange difficult. However, partial metamorphic exchange may account for the late metasomatic influx recorded on the margins of some of the large inclusions. Hewins (1991) also suggested that the Na/Al ratio of chondrules was less susceptible to metamorphic perturbation than the Fa content of olivine or the bulk FeO content of the chondrules. The same may have been true for Na-poor inclusions, which have olivine compositions, but not bulk Na/Al ratios, similar to their hosts.

Another important similarity between large melt objects and chondrules is the pattern of chemical variations for lithophile elements. Chondrules in ordinary chondrites show compositional trends, including positive correlations between Al, Mg#, and Ca, and inverse correlations between Al and Fe (Grossman and Watson, 1983; Weisberg, 1987; Jones and Scott, 1989;

Jones, 1994) that are similar to those for Na-poor melt objects. The observed trends led workers to the conclusion that chondrules formed by the melting of mixtures that contained, in part, (1) refractory, olivine-rich silicates and (2) low-temperature, pyroxene-rich material (Grossman and Wasson, 1982, 1983; Grossman et al., 1988). Various proportions of these two components were presumably responsible for forming olivine-rich and pyroxene-rich chondrules (Grossman et al., 1988). Based on an analogy with large melt objects, it seems possible to assign the high-temperature olivine-rich component to olivine-rich aggregates (OAs), and the low-temperature pyroxene-rich component to material that formed by the removal of OAs from a system with a CI-chondrite-like bulk composition. Ordinary chondrites contain agglomeratic olivine chondrules that may also have been suitable precursors to some chondrules (Weisberg and Prinz, 1996).

4. CONCLUSIONS

Of the three hypotheses for the origin of large, metal-poor, igneous-textured objects in ordinary chondrites, it appears that (1) chondrule formation resulting in the production of large melts and (2) impact melting of chondritic material are both viable. A chondrule-forming process seems especially likely for mega-chondrules, which clearly formed by the solidification of free-floating droplets. Large lithic clasts are texturally more diverse than mega-chondrules, but they appear to have formed by similar geochemical processes and from similar precursors. The large melt objects can be divided into two chemical groups, Na-poor and Na-rich. The compositions of Na-poor objects appear to have been established mainly by vapor-fractionation. An inferred later re-equilibration event at lower temperature, occurring before or during the last episode of melting, raised the Na/Al ratios of the objects to rather uniform, but still low values. In contrast, the compositions of Na-rich objects show no evidence for vapor-fractionation, and instead form compositional trends that resemble those of melt-pocket glasses in ordinary chondrites. Na-rich inclusions may have formed by the incipient-to-complete impact melting of ordinary chondrites. We suggest that Na-poor and Na-rich large melt inclusions correspond to type I/III and type II chondrules, respectively, although additional work is needed to confirm this proposition.

Acknowledgements—The authors wish to thank Marvin Bennett for assistance in preparing Figs. 1–3, David Joy for assistance and use of his SEM facilities, Marty Prinz for generous allocations of samples and hospitality in visits of AR to New York City, Joe Boesenberg for cutting specimens of Julesberg, Mike Weisberg for use of unpublished data, John Wood for making his PHEQ program available, Allan Patchen for assistance with EMP and EDS analyses, and three anonymous reviewers whose comments improved the quality of this manuscript. This work was supported by NASA grant NAGW 3543 to LAT.

REFERENCES

Albee A. L., Quick J. E., and Chodos A. A. (1977) Source and magnitude of errors in broad-beam analysis (DBA) with the electron probe. *Lunar Planet. Sci.* **VIII**, 7–9.

Anders E. and Grevesse N. (1989) Abundances of the elements: meteoritic and solar. *Geochim. Cosmochim. Acta* **53**, 197–214.

Binns R. A. (1967) An exceptionally large chondrule in the Parnallee meteorite. *Mineral. Mag.* **36**, 319–324.

Boss A. P. (1996) A concise guide to chondrule formation models. In *Chondrules and the Protoplanetary Disk* (ed. R. Hewins et al.), pp. 257–263, Cambridge Univ. Press.

Bridges J. C. and Hutchison R. (1997) A survey of clasts and large chondrules in ordinary chondrites. *Meteoritics Planet. Sci.* **32**, 389–394.

Bridges J. C., Franchi I. A., Hutchison R., Morse A. D., Long J. V. P., and Pillinger C. T. (1995) Cristobalite- and tridymite-bearing clasts in Parnallee (LL3) and Farmington (L5). *Meteoritics* **30**, 715–727.

Bunch T. E., Keil K., and Snetsinger K. G. (1967) Chromite composition in relation to chemistry and texture of ordinary chondrites. *Geochim. Cosmochim. Acta* **31**, 1569–1582.

DeHart J. M., Sears D. W. G., and Lofgren G. (1988) Sodium enriched luminescent chondrule mesostases rims in the unequilibrated ordinary chondrites. *Meteoritics* **23**, 265.

DeHart J. M., Lofgren G. E., Jie L., Benoit P. H., and Sears D. W. G. (1992) Chemical and physical studies of chondrite: X. Cathodoluminescence and phase composition studies of metamorphism and nebular processes in chondrules of type 3 ordinary chondrites. *Geochim. Cosmochim. Acta* **56**, 3791–3807.

Dodd R. T. (1978a) The composition of large microporphyritic chondrules in the Manych (L3) chondrite. *Earth Planet. Sci. Lett.* **39**, 52–66.

Dodd R. T (1978b) Compositions of droplet chondrules in the Manych (L-3) chondrite and the origin of chondrules. *Earth Planet Sci. Lett.* **40**, 71–82.

Dodd R. T. (1981) *Meteorites—A petrologic-chemical synthesis*. Cambridge University Press.

Dodd R. T. and Jarosewich E. (1976) Olivine microporphyry in the St. Mesmin chondrite. *Meteoritics* **11**, 1–20.

Dodd R. T. and Jarosewich E. (1979) Incipient melting in and shock classification of L-group chondrites. *Earth Planet. Sci. Lett.* **44**, 335–340.

Dodd R. T. and Jarosewich E. (1982) The compositions of incipient shock melts in L6 chondrites. *Earth Planet. Sci. Lett.* **59**, 355–363.

Dodd R. T, Jarosewich E., and Hill B. (1982) Petrogenesis of complex veins in the Chantonnay (L6f) chondrite. *Earth Planet. Sci. Lett.* **59**, 364–374.

Fodor R. V. and Keil K. (1976a) Carbonaceous and noncarbonaceous lithic fragments in the Plainview, Texas, chondrite: Origin and history. *Geochim. Cosmochim. Acta* **40**, 177–189.

Fodor R. V. and Keil K. (1976b) A komatiite-like lithic fragment with spinifex texture in the Eva meteorite: Origin from a supercooled impact melt of chondritic parentage. *Earth Planet. Sci. Lett.* **29**, 1–6.

Ganguly J. and Tazzoli V. (1994) Fe^{2+}-Mg interdiffusion in orthopyroxene: Retrieval from the data on intracrystalline exchange reaction. *Amer. Mineral.* **79**, 930–937.

Graham A. L. (1993) The Julesberg (L3) meteorite. *Meteoritics* **28**, 122–125.

Graham A. L., Easton A. J., Hutchison R., and Jerome D. Y. (1976) The Bovedy meteorite; mineral chemistry and origin of Ca-rich glass inclusions. *Geochim. Cosmochim. Acta* **40**, 529–535.

Grossman J. N. (1996) The redistribution of sodium in Semarkona chondrules by secondary processes. *Lunar Planet. Sci.* **XXVII**, 467–468.

Grossman J. N. and Wasson J. T. (1982) Evidence for primitive nebular components in chondrules from the Chainpur chondrite. *Geochim. Cosmochim. Acta* **46**, 1081–1099.

Grossman J. N. and Wasson J. T. (1983) Refractory precursor components of Semarkona chondrules and the fractionation of refractory elements among chondrites. *Geochim. Cosmochim. Acta* **47**, 759–771.

Grossman J. N., Rubin A. E., Nagahara H., and King E. A. (1988) Properties of chondrules. In *Meteorites and the Early Solar System* (ed. J. F. Kerridge and M. S. Matthews), pp. 619–659. Univ. Arizona Press.

Hewins R. H. (1991) Retention of sodium during chondrule melting. *Geochim. Cosmochim. Acta* **55**, 935–942.

Hutchison R. et al. (1988) A planetary, H-group pebble in the Barwell, L6, unshocked chondritic meteorite. *Earth Planet. Sci. Lett.* **90**, 105–118.

Ikeda Y. (1983) Major element chemical compositions and chemical types of chondrules in unequilibrated E, O, and C chondrites from Antarctica. *Proc. 8th Symp. Antarctica Meteor., Mem. Nat. Inst. Polar Res. Spec. Issue* **30**, 122–145.

Ikeda Y. and Kimura M. (1985) Na-Ca zoning of chondrules in Allende and ALHA-7703 carbonaceous chondrites. *Meteoritics* **25**, 309–318.

Jarosewich E. (1990) Chemical analyses of meteorites: A compilation of stony and iron meteorite analyses. *Meteoritics* **25**, 323–337.

Jones J. H. (1995) Experimental trace-element partitioning. In *Rock Physics and Phase Relations, A Handbook of Physical Constants* (ed.); *Amer. Geophys. Union* **3,** 73–104.

Jones R. H. (1990) Petrology and mineralogy of Type II, FeO-rich chondrules in Semarkona (LL3.0): Origin by closed-system fractional crystallization, with evidence for supercooling. *Geochim. Cosmochim. Acta* **54**, 1785–1802.

Jones R. H. (1994) Petrology of FeO-poor, porphyritic pyroxene chondrules in the Semarkona chondrite. *Geochim. Cosmochim. Acta* **58**, 5325–5340.

Jones R. H. (1996) FeO-rich, porphyritic pyroxene chondrules in unequilibrated ordinary chondrites. *Geochim. Cosmochim. Acta* **60**, 3115–3138.

Jones R. H. and Scott E. R. D. (1989) Petrology and thermal history of Type IA chondrules in the Semarkona (LL3.0) chondrite. *Proc. 19th Lunar Planet. Sci. Conf.*, 523–536.

Keil K., Fodor R. V., Starzyk P. M., Schmitt R. A., Bogard D. D., and Husain L. (1980) A 3.6-b.y.-old impact melt rock fragment in the Plainview chondrite: implications for the age of the H-group chondrite parent body. *Earth Planet. Sci. Lett.* **51**, 235–247.

Keil K., Stöffler D., Love S. G., and Scott R. D. (1997) Constraints on the role of impact heating and melting in asteroids. *Meteoritics Planet. Sci.* **32**, 349–363.

Kennedy A. K., Hutchison R., Hutcheon I. D., and Agrell S. O. (1992) A unique high Mn/Fe microgabbro in the Parnallee (LL3) ordinary chondrite: nebular mixture or planetary differentiate from a previously unrecognized planetary body? *Earth Planet. Sci. Lett.* **113**, 191–205.

Kieffer S. (1975) Droplet chondrules. *Science* **189**, 333–340.

Kornacki A. S. and Wood J. A. (1984) The mineral chemistry and origin of inclusion matrix and meteorite matrix in the Allende CV3 chondrite. *Geochim. Cosmochim. Acta* **48**, 1663–1676.

Kurat G., Pernicka E. and Herrwerth I. (1984) Chondrules from Chainpur (LL-3): reduced parent rocks and vapor fractionation. *Earth Planet. Sci. Lett.* **68**, 43–56.

MacPherson G. J., Wark D. A., and Armstrong J. T. (1988) Primitive material surviving in chondrites: Refractory inclusions. In *Meteorites and the Early Solar System* (ed. J. F. Kerridge and M. S. Matthews), pp. 746–807. Univ. Arizona Press.

Medaris L. G., Jr. (1969) Partitioning of Fe^{++} and Mg^{++} between coexisting synthetic olivine and orthopyroxene. *Amer. J. Sci.* **267**, 945–968.

Misener D. J. (1974) Cationic diffusion in olivine to 1400°C and 35 kbar. In *Geochemical Transport and Kinetics* (ed. A. W. Hoffman et al.), pp. 117–129. Carnegie Inst. Washington.

Naney M. T., Crowl D. M., and Papike J. J. (1976) The Apollo 16 drill core: Statistical analysis of glass chemistry and the characterization of high alumina-silica poor (HASP) glass. *Proc. 7th Lunar Sci. Conf.*, 155–184.

Papike J. J., Spilde M. N., Adcock C. T., Fowler G. W., and Shearer C. K. (1997) Trace-element fractionation by impact-induced volatization: SIMS study of lunar HASP samples. *Amer. Mineral.* **82**, 630–634.

Prinz M., Weisberg M. K., and Nehru C. E. (1988) Gunlock, a new Type 3 ordinary chondrite with a golfball-sized chondrule. *Meteoritics* **23**, 297.

Rubin A. E. (1994) Metallic copper in ordinary chondrites. *Meteoritics* **29**, 93–98.

Rubin A. E., Keil K., Taylor G. J., Ma M-S., Schmitt R. A., and Bogard D. D. (1981) Derivation of a heterogeneous lithic fragment in the Bovedy L-group chondrite from impact-melted porphyritic chondrules. *Geochim. Cosmochim. Acta* **45**, 2213–2228.

Rubin A. E., Rehfeldt A., Peterson E., Keil K., and Jarosewich E. (1983) Fragmental breccias and the collisional evolution of ordinary chondrite parent bodies. *Meteoritics* **18**, 179–195

Rubin A. E. et al. (1986) Properties of the Guin ungrouped iron meteorite: The origin of Guin and group-IIE irons. *Earth Planet. Sci. Lett.* **76**, 209–226.

Ruzicka A. (1996) Petrologic-kinetic studies of meteorites. Ph.D. Dissertation. Univ. Arizona.

Ruzicka A., Kring D. A., Hill D. H., Boynton W. V., Clayton R. N., and Mayeda T. K. (1995) Silica-rich orthopyroxenite in the Bovedy chondrite. *Meteoritics* **30**, 57–70.

Ruzicka A., Snyder G. A., and Taylor L. A. (1998) Sodium in meteoritic chondrules and large inclusions: Implications for equilibration in the solar nebula. *Earth Planet. Sci. Lett.* (submitted).

Schaal R. B. and Hörz F. (1977) Shock metamorphism of lunar and terrestrial basalts. *Proc. 8th Lunar Sci. Conf.*, 1697–1729.

Schaal R. B., Hörz F., Thompson T. D., and Bauer J. F. (1979) Shock metamorphism of granulated lunar basalts. *Proc. 10th Lunar Planet. Sci. Conf.*, 2547–2571.

Scott E. R. D. and Taylor G. J. (1983) Chondrules and other components in C, O, and E chondrites: Similarities in their properties and origins. *Proc. 14th Lunar Planet. Sci. Conf.*, B275–B286.

Scott E. R. D., Jones R. H., and Rubin A. E. (1994) Classification, metamorphic history, and pre-metamorphic composition of chondrules. *Geochim. Cosmochim. Acta* **58**, 1203–1209.

Sears D. W. G., Hasan E. A., Batchelor J. D., and Lu J. (1991) Chemical and physical studies of Type 3 chondrites— XI. Metamorphism, pairing, and brecciation of ordinary chondrites. *Proc. 21st Lunar Planet. Sci. Conf.*, 493–512.

Sears D. W. G., Huang S., and Benoit P. H. (1996) Open-system behaviour during chondrule formation. In *Chondrules and the Protoplanetary Disk* (ed. R. Hewins et al.), pp. 221–231. Cambridge Univ. Press.

Snetsinger K. G. and Keil K. (1969) Ilmenite in ordinary chondrites. *Amer. Mineral.* **54**, 780–786.

Stöffler D., Bischoff A., Buchwald V., and Rubin A. E. (1988) Shock effects in meteorites. In *Meteorites and the Early Solar System* (ed. J. F. Kerridge and M. S. Matthews), pp. 165–202. Univ. Arizona Press.

Stöffler D., Keil K., and Scott E. R. D. (1991) Shock metamorphism of ordinary chondrites, *Geochim. Cosmochim. Acta* **55**, 3845–3867.

Sylvester P. J., Grossman L, and MacPherson G. J. (1992) Refractory inclusions with unusual chemical compositions from the Vigarano carbonaceous chondrite. *Geochim. Cosmochim. Acta* **56**, 1343–1363.

Taylor L. A., Patchen A., Taylor D.-H. S., and Chambers J. G. (1996) X-ray digital imaging petrography of lunar mare soils: Modal analyses of minerals and glasses. *Icarus* **124**, 500–512.

Vaniman D. T. (1990) Glass variants and multiple HASP trends in Apollo 14 regolith breccias. *Proc. 20th Lunar Planet. Sci. Conf.*, 209–217.

Van Schmus W. R. and Ribbe P. H. (1968) The composition and structural state of feldspar from chondritic meteorites. *Geochim. Cosmochim. Acta* **32**, 1327–1342.

Van Schmus W.R. and Ribbe P.H. (1969) Composition of phosphate minerals in ordinary chondrites. *Geochim. Cosmochim. Acta* **33**, 637–640.

Warren P. H. (1997) The unequal host-phase density effect in electron probe defocussed beam analysis: An easily correctable problem. *Lunar Planet. Sci.* **XVIII**, 1497–1498.

Wasson J. T. (1996) Chondrule formation: Energetics and length scales. In *Chondrules and the Protoplanetary Disk* (ed. R. Hewins et al.), pp. 45–54. Cambridge Univ. Press.

Weisberg M. K. (1987) Barred olivine chondrules in ordinary chondrites: Petrologic constraints and implications. *Proc. 17th Lunar Planet. Sci. Conf., J. Geophys. Res. Suppl.* **91**, E663–E678.

Weisberg M. K. and Prinz M. (1996) Agglomeratic chondrules, chondrule precursors, and incomplete melting. In *Chondrules and the Protoplanetary Disk* (ed. R. Hewins et al.), pp. 119–127. Cambridge Univ. Press.

Weisberg M. K., Prinz M., and Nehru C. E. (1988) Macrochondrules in ordinary chondrites: Constraints on chondrule-forming processes. *Meteoritics* **23**, 309–310.

Wloztka F, Palme H., Spettel B, and Wänke H. (1983) Alkali-differentiation in LL-chondrites. *Geochim. Cosmochim. Acta* **47**, 743–757.

Wood J. A. and Morfill G. E. (1988) A review of solar nebula models. In *Meteorites and the Early Solar System* (ed. J. F. Kerridge and M. S. Matthews), pp. 329–347. Univ. Arizona Press.

Wood J. A. and Hashimoto A. (1993) Mineral equilibrium in fractionated nebular systems. *Geochim. Cosmochim. Acta* **57**, 2377–2388.